# Modeling Water Emission from Intermediate Mass Star Formation Regions

by

Michael Hillier

A thesis
presented to the University of Waterloo
in fulfillment of the
thesis requirement for the degree of
Master of Science
in
Physics

Waterloo, Ontario, Canada, 2008

I hereby declare that I am the sole author of this thesis. This is a true copy of the thesis, including any required final revisions, as accepted by my examiners.

I understand that my thesis may be made electronically available to the public.

## Abstract

In this research water emission is modeled from intermediate mass star formations regions placed at 1 kpc. Nine models are created to describe these regions of varying source luminosity ($L = 100, 500$, and $1000 L_{\odot}$) and protostellar envelope mass ($M = 10, 100$, and $500 M_{\odot}$). For each model, an intermediate mass class 0 protostar is centrally embedded in a spherically symmetry static protostellar envelope. Radiation transfered through these regions is calculated using the program RATRAN that applies an accelerated Monte Carlo method to obtain level population profiles of water. The level populations are used to determine the emission distribution of water from the regions by using a ray tracing method. Strong correlations between line ratios, integrated intensities and source luminosity are found. Larger envelope masses resulted in more mass going in the outer envelope where the water is frozen and does not contribute to the water emission and absorption. Line strengths, ratios, and integrated intensities for all the spectral lines of water within Herschel's observation range are tabulated.

**Acknowledgements**

I would like to extend my deepiest gratitude to my supervisor, Dr. Michel Fich, for his guidance and support throughout the course of this work in addition to giving me the opportunity to be part of his research.

## Dedication

This is dedicated to my parents James and Elizabeth Hillier for their wisdom and endless support.

# Contents

# List of Tables

# List of Figures

# Chapter 1

# Introduction

The research that is presented in this thesis concerns modeling water spectra from star formation regions within the interstellar medium (ISM). In particular, the focus is early stage (no disk) star formation regions containing a class 0 intermediate mass protostar. Regions that will form stars of intermediate mass, defined by final stellar masses of 2-8 $M_{\odot}$, typically have luminosities between $L = 100L_{\odot}$ and $L = 1000L_{\odot}$ [8, 13, 16]. Furthermore, in their earliest star formation stage, intermediate mass stars are surrounded by envelopes of gas and dust having masses between $M_{env} = 10M_{\odot}$ and $M_{env} = 100M_{\odot}$ [1]. Currently, there are studies in the literature that model water lines from low mass star formation regions [17, 21] and high mass star formation regions [3, 6, 7, 20], but no studies concerned with intermediate mass protostars are presently published.

The purpose of this thesis is to complete the modeling of water lines from simplified models of star formation regions, as well as to contribute to our larger understanding of the star formation process. This is accomplished by modeling water lines from the remaining unexplored star formation region, the intermediate mass regime. Protostellar envelopes of class 0 protostars of intermediate mass are modeled. Models are simplified by assuming a spherical geometry and zero velocity field because this significantly reduces the computational time that is associated with modeling these types of regions. If a non-zero isotropic velocity field (eg $v_r = r^{-\alpha}$) was included the overall line profile of the resulting spectra would be similiar. However, the emission peaks would shift further from the center of the line since there is more warmer gas contributing to the emission in comparison to a region that has no velocity field. It is stressed that these simplifications still well represent intermediate mass star formation regions that have been observed in the Galaxy. Water line observations from star formation regions sample very large regions of space where small discontinuities in temperature and density of the medium known to exist in reality have negligible effect. The spherical geometry assumption made in the models "smooth" over density and temperature differences of star formation regions that exist in the Galaxy and therefore do not harm the integrity of the models. To model water lines from more realistic star formation

regions, such as those observed within the ISM, would require computational power that is unavailable at the present.

One of the guaranteed time key programs for the Herschel Space Observatory is called Water In Star-forming regions with Herschel, known as WISH[1]. The objective of the program is to obtain a complete set of water observations from star formation regions containing protostars of all stellar masses. The research presented here is completed at a strategic time, just before Herschel is scheduled to launch (late 2008), providing observers with the only water spectra predictions for intermediate mass star formation regions. Therefore, comparisons can be made between our predictions and observations for these spectral lines so that interpretations can be made for the environments of intermediate mass star formation regions.

In this thesis, water lines are modeled from star formation regions that contain an intermediate mass protostar centrally embedded in a spherically symmetric static molecular cloud. Nine models, of varying source luminosities and envelope masses, were created to describe the intermediate mass star formation regime as mentioned above. Luminosities of $L = 100, 500$, and $1000 L_{\odot}$ were chosen for the source, and envelope masses of $M = 10, 100$, and $500 M_{\odot}$ were chosen for the models. For each model, the molecular cloud is split into many small radial zones (or cells) and a radial temperature profile was calculated using the program DUSTY. In this program some modeling parameters are assumed and specified. These parameters include the protostar's temperature, the power law for the density, and total optical depth straight through the middle of the molecular cloud at $100 \mu m$. Next, the density profiles of gas and water were determined using the density power law and an abundance ratio of water to $H_2$ of $10^{-7}$ for the molecular cloud. Please refer to Chapter 2 for a description of the models. These models are used as input for the RATRAN program. The main RATRAN program, AMC, calculates the radiation that is transferred in the cloud and produces all of the level populations of water in every cell throughout the profile of the cloud. The secondary program of RATRAN, a ray tracing program called SKY, then uses these level populations to map the brightness profile of the cloud onto the sky. Ten lines were selected for investigation and correspond to the observable range of the Herschel Space Observatory. The ten line profiles are obtained from the nine modeled regions which were placed at a distance of 1 kpc. Resulting water lines suffer from large beam dilution since the area of the emitting surface is much smaller than the beam size at this distance and consequently, line strengths are very weak. Furthermore, water lines are excellent luminosity indicators since their integrated intensities, and line ratios of optically thin lines are strongly correlated with luminosity. As for envelope mass indicators, e.g. optically thick lines, the line ratios and ratios of emission peak to absorption temperatures are sensitive to changes in mass; no correlated trends are found for these lines. Future observations of water lines with Herschel will be able to determine the mass of these regions by using many other optically thick lines and taking their line ratios and comparing them with the ones tabulated in this research.

[1] http://www.strw.leidenuniv.nl/WISH/

In this chapter a summary of the important properties of water will first be presented to explain why it serves as an excellent environmental probe for star formation regions. Second, the current picture of the star formation process will be described as well as any remaining questions and problems associated with that picture. Lastly, the observational tools and difficulties with detecting water emission will be presented. This includes a general overview of Herschel, the first space observatory that will fully cover the far infrared and sub mm portions of the electromagnetic spectrum.

## 1.1 Water

Water is one of many different molecules that can be used as an environmental probe for star formation regions. However, it serves as one of the best molecules to probe these types of environments. This is directly related to the fact that water has some "special" properties. Moreover, star formation regions of all types may contain large amounts of solid and/or gaseous forms of water [20]. In the cooler ($< 20K$) parts of these regions, the protostellar envelopes, $O$ and $H$ atoms can combine on dust grains to form water ice. When gas temperatures are $> 250K$ most of the gaseous oxygen that is not converted into $CO$ is converted into water by its reactions with $O$ and $OH$ [20].

Water is a very complicated and interesting molecule because its principle moments of inertia are all different. These types of molecules are referred to as asymmetric top molecules and rotate differently than simpler types of molecules such as $CO$ or $CN$. Furthermore, due to the fact that there are multiple possible configurations for the nuclear spins on the hydrogen atoms, water has two different "flavors", ortho and para. Ortho water has the nuclear spin on $H$ atoms parallel to one another, whereas, para water has its nuclear spins on hydrogen atoms anti-parallel. The ratio between these two forms is $3(ortho) = 1(para)$ at high temperatures ($> 50K$). At lower temperatures ($< 50K$), the ratio is different and only approaches 3:1 with increasing temperature. The fact that all the principle moments of inertia are different for water gives rise to a wide variety of observable lines. Specifically, there are many optically thin and thick lines that potentially provide velocity, temperature, and density information from the region from which they originate from. It is therefore possible to obtain a complete inventory of environmental parameters associated with a particular star formation region by using water emission.

## 1.2 Star Formation

Stars are born from dense regions of gas and dust in the ISM. Their lifetimes are dependent on their mass: the more massive a star the shorter its lifetime. Upon the death of a star its material is injected into the ISM enriching the medium where

future stars will be born. There are two ways in which this can occur and they are dependent on the mass of the dying star. For stars of low mass the envelope expands to the point where the star loses its envelope which is slowly returned to the ISM. For massive stars, a supernova explosion can occur in which the explosion injects the stars material into the ISM within an instant.

In the ISM, clouds of molecular gas and dust are collected through a variety of different ways. For example, high density regions of gas and dust gravitationally attract more gas and dust from their surrounding environment than regions of lower density.

For simplicity, consider a spherically symmetric molecular cloud of uniform density and temperature. Using the virial theorem, the cloud is at equilibrium when $2K = |U|$ (K is the kinetic energy of the cloud and U is the gravitational energy). If $2K > |U|$ the cloud expands; on the other hand, when $2K < |U|$ the cloud collapses. It can be shown that the minimum mass enclosed by some radius required to initiate gravitational collapse is given by the following expression

$$M_J = \left\{ \frac{5KT}{G\mu m_H} \right\}^{3/2} \left\{ \frac{3}{4\pi\rho_o} \right\}^{1/2} \tag{1.1}$$

where T is the temperature of the cloud, $\mu$ is the mean molecular weight, $m_H$ is atomic mass of hydrogen, and $\rho_o$ is the mass density of the cloud. Once the mass of the cloud exceeds $M_J$, the "Jeans mass", the gravitational force is greater than the kinetic energy and the cloud begins to collapse. The collapse is initially isothermal as long as the cloud remains optically thin to the infrared radiation (primarily from dust) that is dominant within such clouds. As the cloud's size decreases during the collapse its density and pressure increase. Since a spherical cloud is more dense in its center and its free-fall time scale associated with this location is smaller than the outer parts of the cloud the density at the center increases more rapidly than the outer regions. Once the density of the material near the center approaches $10^{-13} gcm^{-3}$ the central region becomes optically thick in the infrared [4]. As a result, the collapse becomes more adiabatic near the center and the central temperature increases to about $2000K$ [4]. As the temperature and pressure increase the collapse near the center slows and the condition of hydrostatic equilibrium is established. This defines a core that thermally supports its surrounding protostellar envelope. This is the birth of a protostar. This is the point of the star formation process that is modeled in the research presented in this thesis. The sequence and details of these events are illustrated in Figure 1.1.

After the birth of the protostar, matter is accreted onto the central region from the surrounding protosteller envelope. In this stage a protoplanetary disk is formed if the cloud has a sufficient amount of angular momentum. The envelope is extremely optically thick at this time, and only the outer regions of the envelope can be observed in infrared wavelengths. Furthermore, it has been observed that bipolar outflows, perpendicular to the disk, are created at this stage of the evolutionary sequence. As time evolves these outflows blow away some of the matter belonging

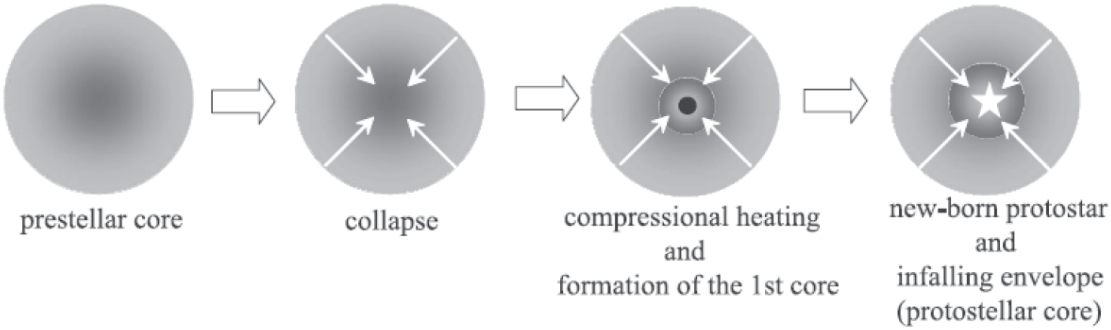


Figure 1.1: The formation of the protostellar core.

to the region back into the ISM, a process that lowers the optical depth. When the accreting envelope becomes transparent to optical light a T Tauri star is found at its central location. This young stellar object (YSO) is in the pre-main sequence stage of its evolution. Moreover, as the protostar continues to contract its temperature increases slowly and creates convective zones in the remaining envelope. Once the temperature of the protostar increases to the point where thermonuclear fusion can occur for hydrogen, hydrogen begins to be converted into helium. This is the point where the star enters the main sequence as a zero age main sequence star (ZAMS). The main sequence is where the star will spend the majority of its lifetime.

Currently, our understanding of the star formation process needs improvement since questions still remain regarding particular details of the process. This is due to the fact that there are observational difficulties encountered when observing optically thick regions like those in early stage star formation regions. To resolve these difficulties, astrophysicists look for radiation coming from star formation regions in the sub mm regime of the electromagnetic spectrum. Radiation at these wavelengths are very useful since the wavelengths are long enough to avoid being scattered or absorbed by other gas particles. Therefore, radiation at these wavelengths escapes the regions allowing astronomers to observe and probe these types of environments. Water, for example, is an molecule that radiates at these sub mm wavelengths.

The central problem with the current star formation picture is understanding how the mass of a new born star is correlated with the mass/density of its star forming molecular cloud. The other big question that remains regarding the star formation process is how star forming molecular clouds of a certain size and mass create a distribution of stars with different masses. One of the processes related to this phenomena is refered to as the fragmentation process. Specifically, fragmentation is the process in which many parts of a molecular cloud individually satisfy the Jeans mass and collapse to form multiple protostars in the same cloud. This is clearly seen observationally since stars are frequently found to have many close neighbouring stars ranging from a few stars to clusters having thousands of members. Moreover, there are puzzling aspects of the fragmentation process. In

particular, it is unclear how the fragmentation process creates many more smaller objects than larger objects. The key to unlocking this mystery is to follow the changes of environments of star formation regions at the different stages of their evolution. Using water observations correlations between the mass of the forming star and environmental parameters (density, molecular abundances, temperature) of its surrounding medium can be found. In this research we modeled intermediate mass star formation regions at a early stage (no disk) surrounded by a protostellar envelope whose density followed a density power of index 1.5, that has no systematic velocity field. If our modeled water lines from these regions have similar structures and line strengths to the observations taken from candidate regions in our galaxy then our modeling conditions (temperature, density, abundance and size) would be accurate. Undoubtedly, water will be used to develop our understanding of the star formation process and the environmental conditions of star formation regions. This research provides some of the necessary ground work required for accomplishing this.

## 1.3 Observing Water Lines

The major difficulty encountered when observing water emission from intergalactic star formation regions is that they can only be observed from space. This is due to the fact that water in the Earth's atmosphere absorbs all water emission originating from space. It is therefore necessary to launch an observatory in orbit around the Earth to observe the radiation. There have been three observatories launched into space relatively recently (1995-2001), including the ISO, ODIN, and SWAS satellites that are able to observe water emission. These earlier sub mm observatories, however, suffered from low spatial resolution as well as the inability to tune to many different frequencies.

The Herschel Space Observatory on the other hand, to be launched in late 2008, will have a very high resolution heterodyne spectrometer with the ability to observe at least 32 different water lines [5]. This will allow a full inventory of environmental parameters, such as temperatures, molecular densities, velocities, and chemistries of star formation regions to be taken, enabling researchers to understand these environments. The hope is to understand how particular environments favor the formation of specific types of stars so that the star formation picture can be complete.

## 1.4 Structure of Thesis

Chapter Two describes the intermediate mass star formation regions which have been modeled in this research and also describes the details for how the models were created. Chapter Three describes the theory on which this research is based, specifically, the physics of quantum rotational transitions of molecules and the

radiative transfer process in star formation regions. In Chapter Four our results, modeled water lines from intermediate mass star formation regions, are presented and analysed for trends with envelope mass and source luminosity. In Chapter Five, I discuss my conclusions.

# Chapter 2

# Modeling

There are two distinct types of radiative transfer modeling carried out in this research. First, we model the environments of protostellar envelopes containing an embedded intermediate mass protostar given parameters which have been observed for these types of regions within the Galaxy [1, 3, 8, 13, 15, 16, 18]. To determine the temperature profile the radiative transfer from the dust continuum was modeled. The assumption that the $H_2O$ cooling is much less than the dust cooling is used when modeling the radiative transfer of the dust continuum. Second, by using a Monto Carlo method, the radiation transferred and molecular excitation of $H_2O$ are modeled for these molecular clouds. The excitation of $H_2O$ comprises the bulk of the modeling implemented in this research. In this chapter, the procedure of modeling the environmental parameters of the star formation regions of interest is first presented. Finally, our method for modeling the process of radiative transfer and excitation of $H_2O$ in these regions is dicussed in the last half of this chapter.

The modeling presented in this thesis only encapsulates a small portion of the total amount of research carried out in the process of completing this work. The research material not presented in this thesis, the preparatory research, was the work that was required to obtain integrity in the current models. Extensive work was required to investigate parameter space for input parameters that describe our models in the DUSTY program, in addition to the input parameters for RATRAN and SKY. For example, we explored the effect of increasing the resolution of radial zones in the protostellar envelope and its effect on the final output, the spectral lines of water. The number of "zones" or cells were increased to 1000 which in effect dramatically increased computing time for RATRAN. For models consisting of 100 cells typically take $\tilde{2}$ days to compute while models consisting of 1000 cells take up towards 3 months to compute.

## 2.1 Modeling Intermediate Mass Star Formation Regions

In this section the method of modeling intermediate mass star formation regions is presented. As mentioned in the introduction chapter, we represented the intermediate mass star formation regime with 9 models. Each model is described by a source luminosity and envelope mass and not by the protostar's stellar mass. A source luminosity, $L = 100$, or 500, or $1000L_{\odot}$ is chosen for the protostar and a mass $M = 10$, or 100, or $500M_{\odot}$ is chosen for the envelope of gas and dust around the protostar. Note that envelope masses of $500M_{\odot}$, an envelope mass which larger than the observed range for the intermediate mass regime, are included in our models. This is done to take into account the possibility that envelope masses may be larger than the observed range which is based on a very limited set of observations. Specifically, we modeled spherical protostellar envelopes surrounding a centrally embedded class 0 intermediate mass protostar as illustrated in Figure 2.1. The models are required to describe the $H_2$ and $H_2O$ number density profiles (density as a function of radius) of these regions in addition to its temperature and any possible velocity fields associated with these regions. The methods for calculating the temperature and density profiles for protostellar envelopes are discussed. At the end of the section the interpolation method used for the models is presented. Interpolation is required for our models since higher resolution is needed than the very low resolution data obtained from a program used early in the modeling procedure.

### 2.1.1 Temperature profiles

The first step for modeling intermediate mass star formation regions is to obtain a temperature profile for the surrounding protostellar envelope. To accomplish this the program DUSTY [10] was used. The program calculates the radiative transfer in dust continuum radiation of regions possessing spherical or planar geometries, and outputs an array of different variables, one of which is temperature and its variation with position. DUSTY splits the modeled region into many radial cells that are logarithimicaly spaced, as illustrated in Figure 2.1. Version 2.06 of the program was used since it allowed us to specify the input parameters we wanted to control. These input parameters include the luminosity and temperature of the source, the size of the cloud, the cloud's optical depth, the power law index for the density distribution, the dust grain size distribution, and external heating from an interstellar radiation field (ISRF) [2]. The temperature of the central source (the surface of the protostar) in all the models was fixed at $T = 2500K$. In addition, the optical depth at $100\mu m$ for all the envelopes was fixed at $\tau_{100} = 0.1$. For optical depths on the order of $\tau_{100} = 0.1$ and lower the central source is the dominant contributer to the envelope's radiation, instead of heating from diffuse fields reemitted by the dust grains. It is more physically realistic to have the radiation field driven by the central source rather than heating from dust grains in its surrounding

environment. Furthermore, models in which lower values of $\tau_{100}$ are used resulted in gas densities that were much lower than what has been observed from star formation regions in the galaxy (e.g. $n_{H_2} = 10^6\ cm^{-3}$ on the inner regions of the envelope [8, 13, 15]).

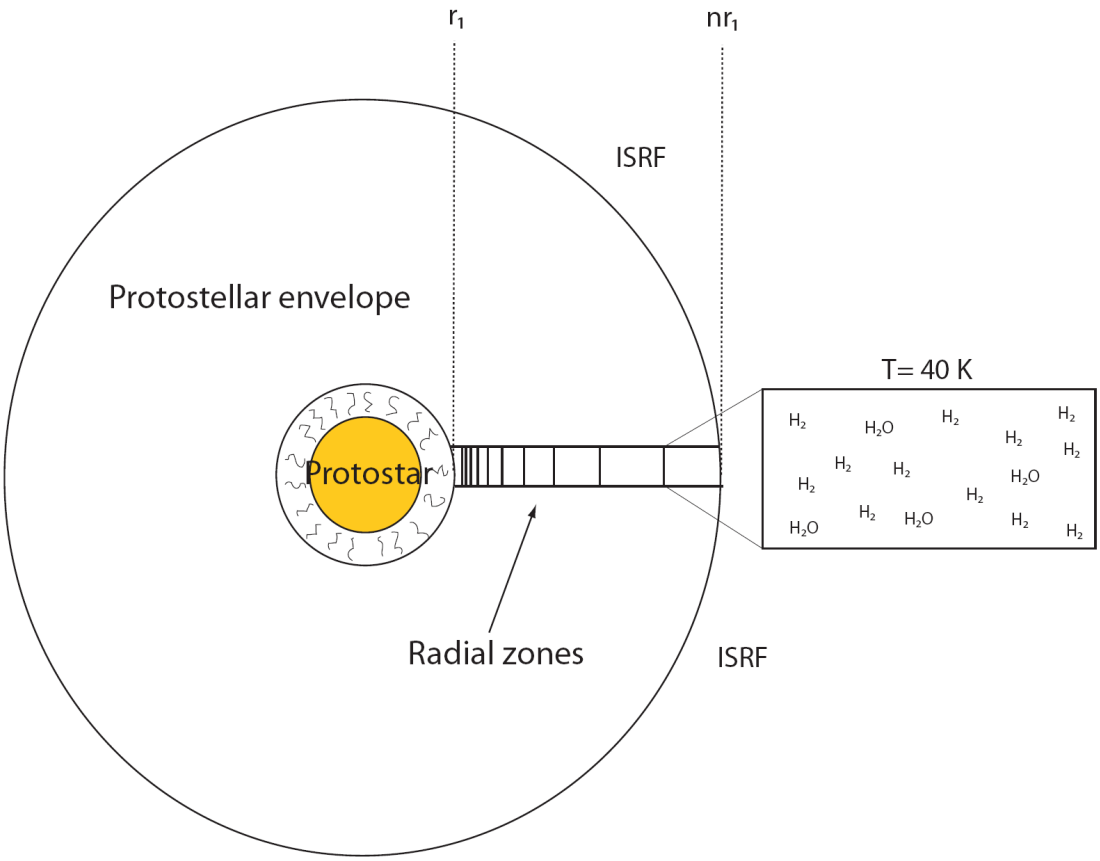


Figure 2.1: Structure of modeled regions. Logarithmic spacing of radial zones, or cells, is shown for a particular slice of the region. The temperature, molecular densities, and velocity are specified in each cell of the input model.

The first set of input parameters that is required for DUSTY is the luminosity of the embedded protostar and the radius at which dust sublimates in its protostellar envelope, $r_1$. An initial estimate of $r_1$ $10^{14}$ cm was made, and the program was run. The program calculates a temperature profile for that given model as a function of scaled radius, defined by

$$y = \frac{r}{r_1}. \tag{2.1}$$

Subsequent adjustments to $r_1$ was made until the temperature at $y = 1$ (e.g. $T_1$) is 300 K, since dust is destroyed at this temperature [17, 21]. This temperature is a critical parameter. We expect significant increases to line strengths if $T_1$ is set to higher values (eg. 700 K). Once the right $r_1$ was achieved to produce 300 K at

| Input Parameters for DUSTY | | | | |
|---|---|---|---|---|
| Model | L ($L_\odot$) | $M_{env}$ ($M_\odot$) | $r_1$ ($\times 10^{14}$)(cm) | n ($\times 10^3$) |
| Model 1 | 100 | 10 | 3.18 | 5.44 |
| Model 2 | 500 | 10 | 7.10 | 1.85 |
| Model 3 | 1000 | 10 | 10.0 | 1.17 |
| Model 4 | 100 | 100 | 3.18 | 25.4 |
| Model 5 | 500 | 100 | 7.10 | 8.66 |
| Model 6 | 1000 | 100 | 10.0 | 5.48 |
| Model 7 | 100 | 500 | 3.18 | 74.3 |
| Model 8 | 500 | 500 | 7.10 | 25.4 |
| Model 9 | 1000 | 500 | 10.0 | 16.1 |

Table 2.1: Input parameters for DUSTY for the 9 models. $T_{source} = 2500K$, $T_1 = 300K$, $\tau_{100} = 0.1$, and 1.5 power law index for the density distribution were fixed for all models.

$y = 1$ the outer radius , $r_{outer}$, given by

$$r_{outer} = nr_1, \tag{2.2}$$

of the protostellar envelope has to be determined to produce the required envelope mass, $M_{env}$, that was assigned to that model. This is done by solving the derived equation for the total mass of the dust in a spherical cloud with a 1.5 power law index and a MRN [14] grain size distribution for $n$

$$M_{dust} = \frac{M_{H_2}}{100} = \frac{4\pi\tau_\lambda}{3\kappa_\lambda} \frac{(nr_1)^{3/2} - (r_1)^{3/2}}{(r_1)^{-1/2} - (nr_1)^{-1/2}}. \tag{2.3}$$

In the above equation $\kappa_\lambda$ is the envelope's opacity at wavelength $\lambda$, $\tau_\lambda$ is the optical depth at wavelength $\lambda$ straight through the center of the region, and the ratio between $M_{dust}$ and $M_{H_2}$ is assumed to be 1:100. Once $n$ is determined, the input parameter (in the DUSTY input file containing all the input parameters for that given model) for the outer radius of the protostellar envelope was set to this value (note: changing $n$ has neglible effects on $T_1$). The program was run again using the determined input parameters as discussed above and the final temperature profile for that model was obtained, assuming that $T_{gas} = T_{dust}$. The array of input parameters used for DUSTY to create the temperature profiles of the nine models is summarized in Table 2.1.

Temperature profiles for the nine models are presented in Figure 2.2. Temperature curves are grouped according to protostar luminosity. Different line types represent a particular protostar's luminosity. The 3 different coloured curves with the same line type have envelopes with different masses. Three behaviours on the plot are noted. First, larger luminosity of the central source result in a hotter temperature profile. Second, all models with the same source luminosity but different

envelope masses have the same temperature profile. Since the radiation fields of protostellar envelopes are dominated by the central source, models having the same source luminosity will also have the same temperature profile. Third, for all models, the temperature near the edge of the molecular cloud converges to the temperature of the exterior boundary condition, the temperature due to the external interstellar radiation field $T_{outer} = 13.8$K.

### 2.1.2 Density Profiles

As mentioned previously, the density profiles for the models are assigned a power law with a 1.5 index. This power law describes the density profiles of a dense isothermal sphere [19]. It can be shown that the number density of $H_2$ as a function of radius for spherically symmetric static molecular clouds is given by

$$n_{H_2} = a\frac{\tau_\lambda}{\kappa_\lambda r^{3/2} u}\frac{1}{(r_1)^{-1/2} - (nr_1)^{-1/2}} \tag{2.4}$$

where u is the atomic mass unit, and $a = \frac{H_2}{dust}\frac{1}{(Integration\ constant)\times(\#atoms\ in\ H_2)} = \frac{100}{1}\frac{1}{2\times 2} = 25$. The $H_2$ density profiles for the nine models are presented in Figure 2.3.

Determining the number density of water as a function of radius is done by multiplying the number density of $H_2$ by the abundance of water relative to $H_2$. This abundance, however, does not presently have tight constraints due to the limited water observations taken thus far from these types of regions within the Galaxy. From these, it appears that this abundance lies in the range of $10^{-6}$ to $10^{-8}$ [11,22]. For our models we have chosen the value $10^{-7}$. Another important feature in the water density profiles is the freezeout point of water. Water is completely frozen out on dust grains at temperatures $\leq 20K$ and this in effect halts all water emission in the outer parts of the molecular cloud. To account for this behaviour in our models the number density of water in freezeout zones are multiplied by $10^{-5}$. This value was chosen because smaller values produced a numerical instability in AMC code while larger values produced a small amount of water emission in the freezeout zone.

### 2.1.3 Interpolation methods

The program DUSTY, used to create the temperature profiles for the models, produces a small number of radial cells. Hence, poor temperature and density resolution is obtained for the models over the profile of the protostellar envelope. The number of cells that are generated by DUSTY is dependent upon the optical depth of the region being modeled: the number of cells increases with increasing optical depth. For the 9 models, as described earlier, the optical depth $\tau_{100} = 0.1$ was used. The number of data points produced by DUSTY for the 9 models was between 25

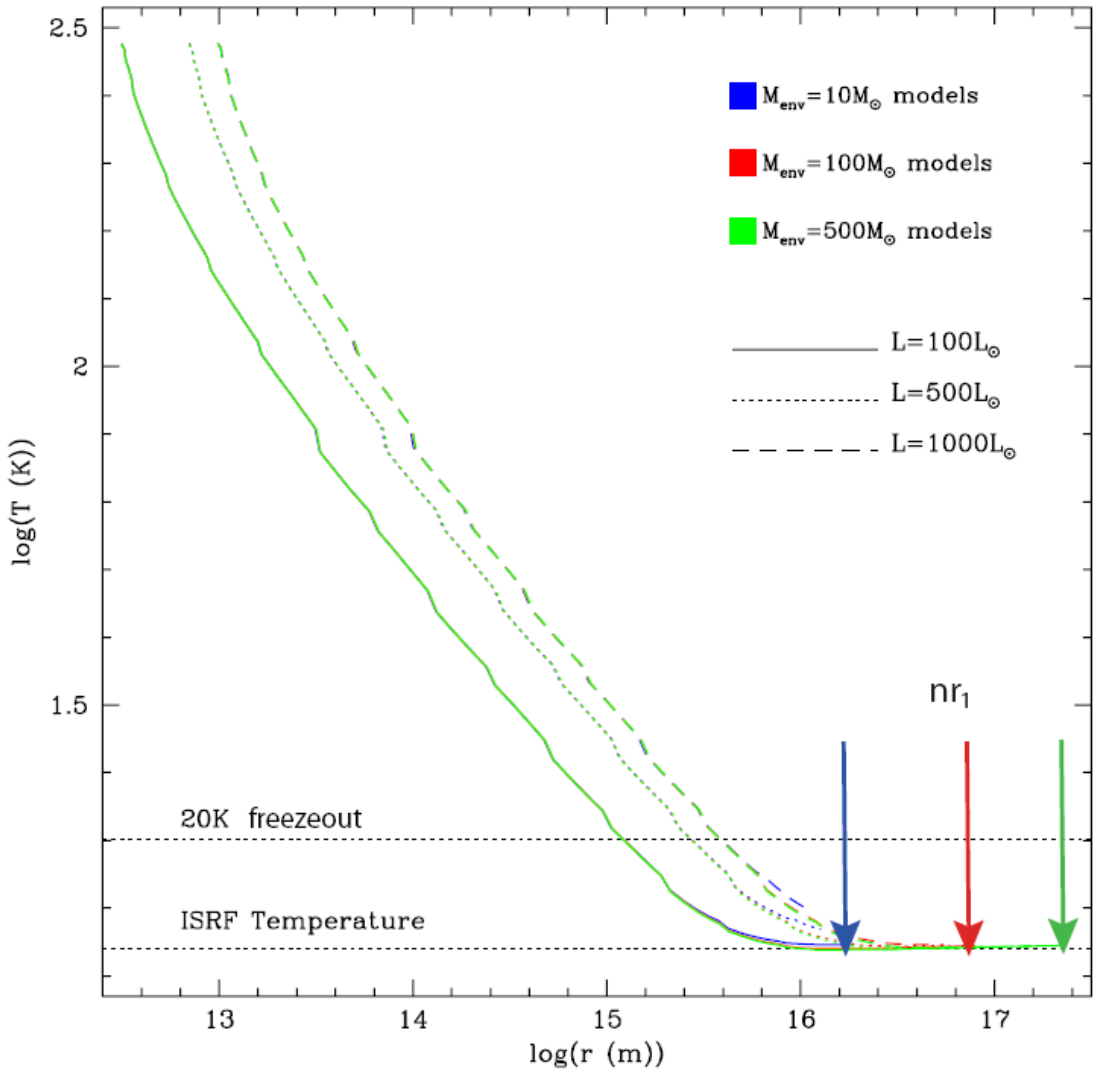


Figure 2.2: Temperature dependence with radius for nine investigated models. Coloured curves represent protostellar envelopes of different masses and line types represent protostar sources of different luminosities. Uncoloured dotted lines represent the temperatures of the water freezout point and the interstellar radation field (ISRF). Coloured arrows represent $nr_1$, the outer radius of a protostar's envelope, for the models (dependent on $M_{env}$).

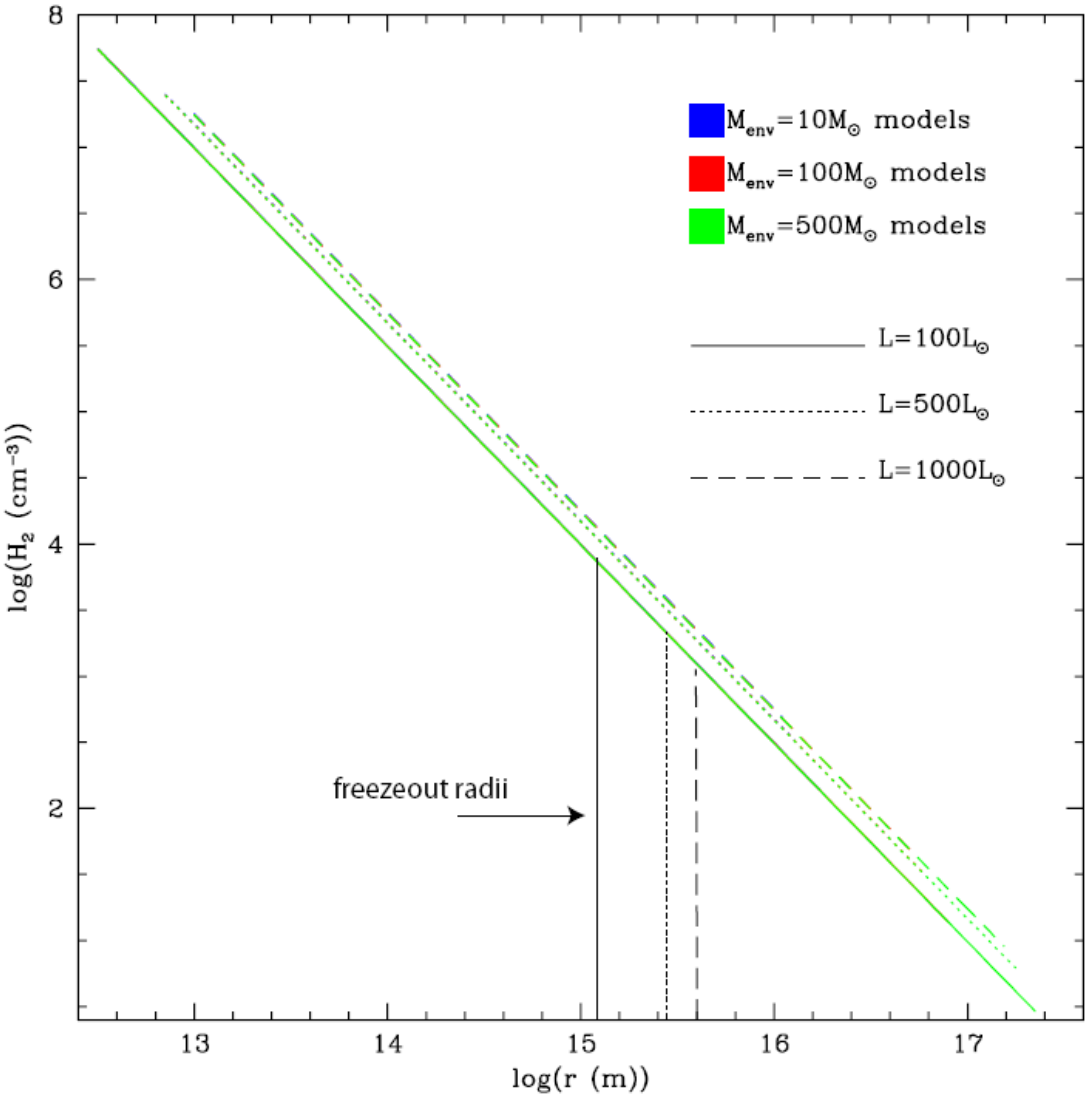


Figure 2.3: Radial dependence of $H_2$ density of the nine models. Vertical lines represent the freezeout radii for the models. Freezeout radii are the same for models of the same source luminosity.

and 30. The low numbers of cells are distributed over a large radial range (as large as 74000× the inner radius). Higher resolution is therefore required to produce a more realistic picture of the physics exhibited by these regions. To obtain higher resolution a cubic interpolation scheme, written in Fortran 77, was used on the output data from DUSTY (see Appendix for code). The effect of resolution and the requirement for some minimum number of data points are clearly seen from the evolution of the level population of water as a function of the normalized cell number, y, as the number of cells used for a particular model is increased. This is clearly illustrated in Figure 2.4. Models having $\sim 100$ cells are sufficient to replicate the nature of the radiation field since models having over 100 cells produced minimal changes to the overall level population profile of water.

## 2.2 Radiative Transfer and Molecular Excitation Modeling

The radiative transfer of water and its molecular excitation comprise the bulk of our modeling. In addition, these represent the core physics incorporated into this research and for this reason a summary of the code that is used to modeled these processes is presented. The code, RATRAN, developed by Michel Hogerheijde and Floris van der Tak [9] is used. The program calculates the radiative transfer and molecular excitation in regions that posses spherical symmetry: this is a 1D radiative transfer code. RATRAN consists of two programs: AMC which stands for Accelerated Monte Carlo and SKY which is a ray tracer program. An input model that subdivides the spherical region into many radial cells is supplied to the program. The input model, as described in the first half of this chapter, is required to describe the molecular number densities, gas temperature, and velocity field profiles for the region. The code applies an accelerated Monte Carlo method to iteratively converge on the mean radiation field, $J_\nu$, for the molecular cloud. All level populations of the molecule of interest can then be calculated once $J_\nu$ is determined for every cell distributed throughout the profile of the cloud. Furthermore, these level populations are required to map the emission distribution from the investigated region on the sky.

### 2.2.1 AMC

The AMC program is a one dimensional code that determines the radiation field of the modeled region through the following procedure. Since we are investigating spherically symmetric regions this code suits the research because the information in one direction is simply integrated over the volume of the sphere. The program calculates two quantities, the mean radiation field and the average level populations of water in every radial zone, throughout the region being studied. This is accomplished by following photons emitted by the water molecules. Our protostellar envelopes are fragmented into radial cells, all of which contain the appropriate

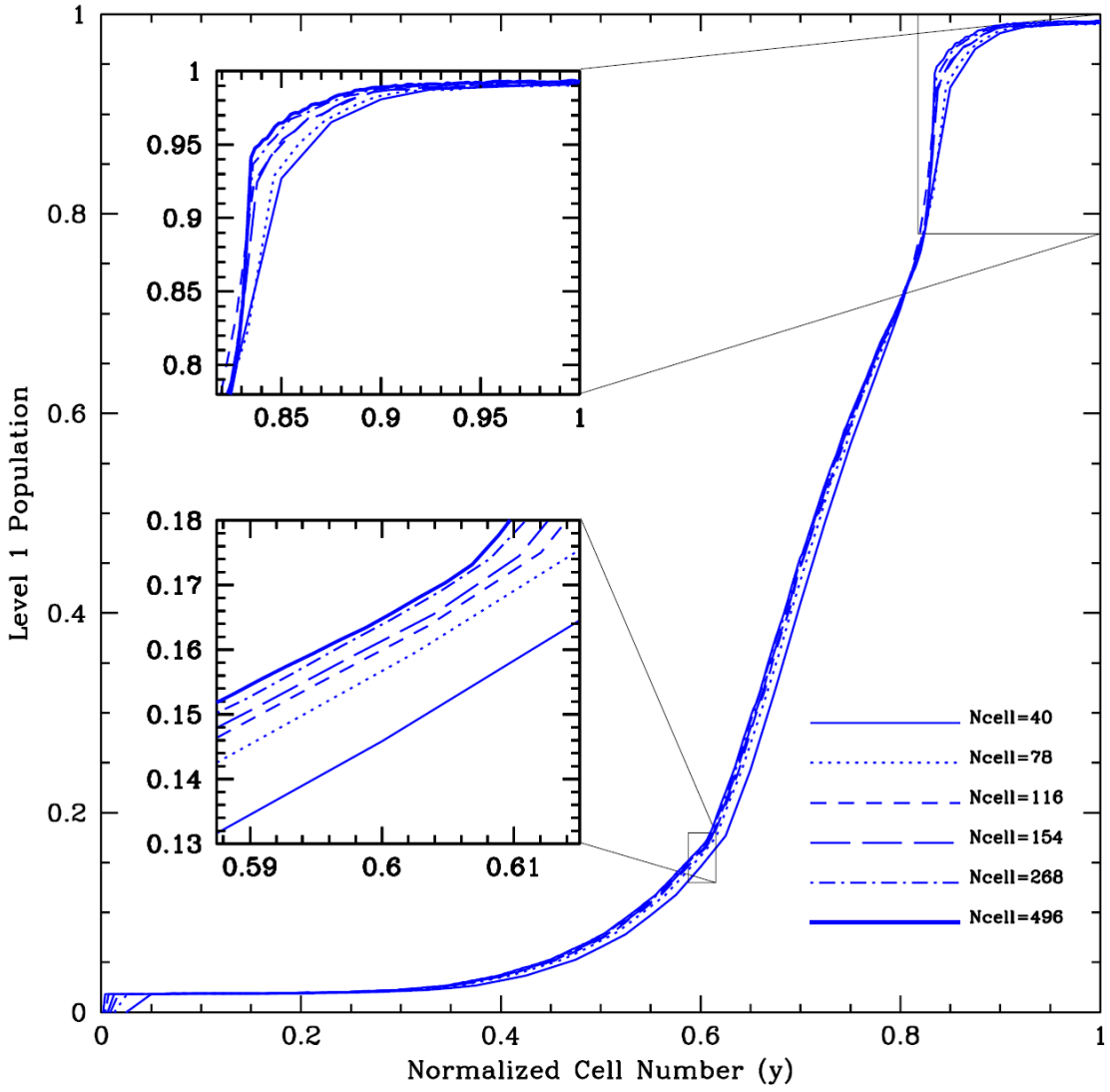


Figure 2.4: The level 1 populations of water molecules in cloud envelope as a function of ncell (number of cells distributed over the radial range of spherical cloud) is presented. Level populations converge with increasing ncell. Converging behaviour shown in insets A) and B), the two areas in the cloud where population of level 1 changes the most with varying ncell.

environmental information. First, the sampled number of rays (user specified) are randomly distributed throughout each cell in the input model and the rays are pointed in random directions; since this program is only 1 dimensional there are only two possible directions. Second, the distance from each ray's origin to that cell's boundary is determined. Third, with this distance known the incident intensity along the ray at every cell edge is calculated through the radiative transfer equation. Please refer to Chapter 3 for the explict details regarding the theory behind the radiative transfer. Furthermore, the attenuation of intensity encountered by rays as they pass through cells along its path are taken into account. In addition, traveling rays change direction randomly from cell to cell which in turn modifies the line profile function. RATRAN calculates the mean radiation field for every cell using the information provided by the sampled rays from every cell in the input model. These mean radiation fields are then used to produce the average level populations of water throughout the profile of the region through the statistical equilibrium equation. Run times for this program are dependent on the program's input parameters. The parameters that have the biggest effect on run times are the number of radial zones (number of cells) the modeled region has as well as the number of sampled photons used. Increasing these parameters increases the run times dramatically as well as increasing the accuracy of the calculation. The sufficient number of sample photons is on the order of a thousand. Exceeding the number of cells beyond 1000 will produce run times around 3 months.

### 2.2.2 SKY

Mapping the emission from an ensemble of molecules changing different rotational energy states within a particular medium requires level populations of those states to be known throughout that medium. For our investigated regions the averaged level populations of water in every cell distributed in the molecular clouds are determined using the program AMC as stated above. Combining the water density and level population information in a given cell allows the intensity of the transitions (i.e. the emission) to be determined for that cell. The program calculates these intensities in terms of brightness temperatures and takes many velocity slices of the molecular cloud and then outputs the data to a 3D (2 spatial and 1 velocity dimension) "FITS" (Flexible Image Transfer System) image. To obtain spectra for the transitions from these regions the image is convolved to an observing beam size at some known distance.

# Chapter 3

# Theory

In this chapter the theory and physical processes at the core of this research are presented. The results from the research, e.g. the spectral lines of water, are produced via the process of quantum rotational transitions. Environmental conditions of a region greatly influence the nature of these transitions. This chapter contains two main sections. In the first section, quantum rotational phenomena are described to explain how rotational spectra are created [12]. In the last section of this chapter, the process of radiative transfer in molecular clouds is described to explain how the molecular excitation process works. Collectively, using the information presented in this chapter environmental variables such as temperature, densities, abundance, velocity can be determined from the analysis of rotational spectra.

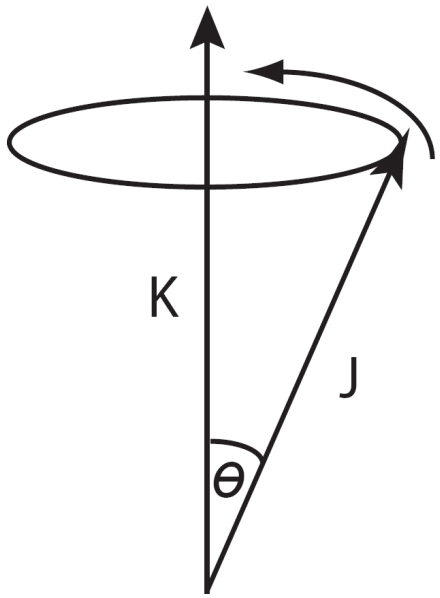


Figure 3.1: Diagram for the total angular momentum **J** and symmetric axis vectors **K**.

## 3.1 Quantum Rotational Transitions

A quantum rotational transition is the process by which molecules change quantized rotational energy states. These energy states are represented by the quantum numbers $J_{K^+K^-}$, where **J** is the total angular momentum and $K^+$ and $K^-$ are the projections of **J** onto the symmetric axis **K** as illustrated in Figure 3.1. Difficulties are generally encountered when investigating rotational transitions for molecules because one has to consider all possible vibrational transitions at the same time if the bond lengths between atoms of a molecule change with respect to time. For cold systems, like molecular clouds, vibrational motion is neglible and only rotational transitions influence the spectra. In addition, energy level diagrams summarize all the quantum phenomena exhibited by a particular molecule. Water's energy level diagram is shown in Fig. 3.2 . Therefore, the primary objective to any investigation where rotational transitions are present should be obtaining and understanding the energy level diagrams for molecules undergoing these transitions. The first step is to characterize that molecule's energy.

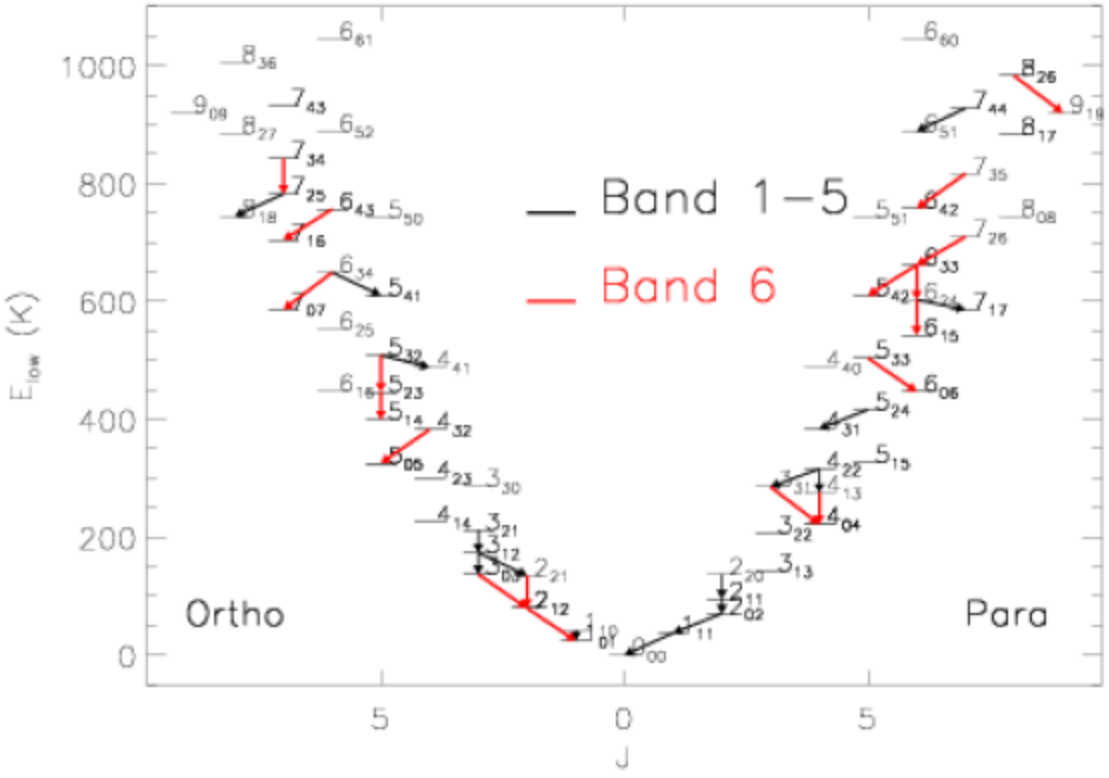


Figure 3.2: The energy level diagram for both $o-H_2O$ and $p-H_2O$ for energies up to 1000 K. Arrows indicate Herschel's observable transitions along with their corresponding band passes.

Consider a cold $H_2O$ molecule in free space (V=0) with its center of mass located at the origin of a Cartesian coordinate reference frame (lab frame) as illustrated

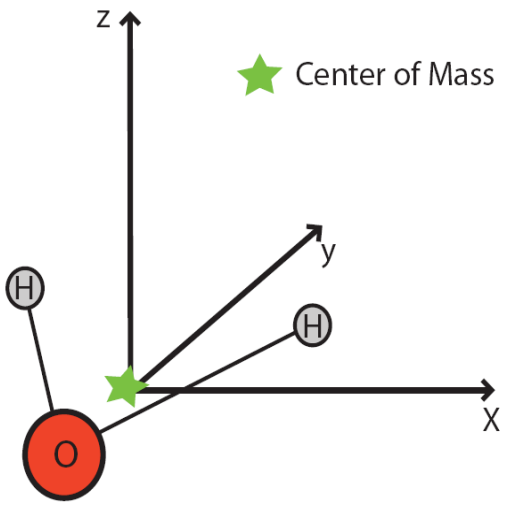


Figure 3.3: Molecular diagram for a fixed Cartesian axis.

on Figure 3.3. The molecule also has a rotating Cartesian frame fixed to it. The molecule's rotational energy, represented by a rotational Hamiltonian, $H_r$, is given by

$$H_r = T_r = \frac{1}{2} I_{\alpha\beta}\omega_\alpha\omega_\beta \tag{3.1}$$

where $T_r$ is the rotational kinetic energy, $I_{\alpha\beta}$ are the elements of inertia tensor, and the $\omega$'s are the angular speeds about a particular axis. The repeated indices allow Einstein summation notation. The moments of inertia tensor $I_{\alpha\beta}$, is given by

$$I_{\alpha\beta} = \begin{bmatrix} I_{aa} & I_{ab} & I_{ac} \\ I_{ba} & I_{bb} & I_{bc} \\ I_{ca} & I_{cb} & I_{cc} \end{bmatrix}$$

where a, b, and c are the orthogonal axes for the molecule fixed frame. For molecules that only rotate (no vibrational motion included) the rotational Hamiltonian can be written in terms of rotation about the molecule-fixed axes a, b, and c. Each element of the moments of inertia tensor, $I_{\alpha\beta}$, can be determined through the following equations

$$I_{aa} = \Sigma_i m_i[r_{ib}^2 + r_{ic}^2] \qquad I_{ab} = -\Sigma_i m_i[r_{ia}r_{ib}] \tag{3.2}$$
$$I_{bb} = \Sigma_i m_i[r_{ia}^2 + r_{ic}^2] \qquad I_{bc} = -\Sigma_i m_i[r_{ib}r_{ic}] \tag{3.3}$$
$$I_{cc} = \Sigma_i m_i[r_{ia}^2 + r_{ib}^2] \qquad I_{ca} = -\Sigma_i m_i[r_{ic}r_{ia}] \tag{3.4}$$

It can be shown that the Hamiltonian is

$$H_r = \frac{1}{2}\mu_{\alpha\beta}J_\alpha J_\beta \tag{3.5}$$

where $\mu_{\alpha\beta}$ is an element of the tensor $I^{-1}$. This tensor is diagonalized by any unitary transformation matrix $U$ such as

$$\mathbf{U} = \begin{bmatrix} cos\theta & sin\theta & 0 \\ -sin\theta & cos\theta & 0 \\ 0 & 0 & 1 \end{bmatrix}$$

where $\theta$ is the angle of rotation of a coordinate system relative to another coordinate system. For the molecule there is an orientation for the axes such that the cross product terms of Eqn. 3.1 and Eqn. 3.5 are zero. In this special orientation, the axes are called the Principal Axes and the three diagonal elements of the tensor **I** are known as the Principal Moments of Inertia. Let the Principal Moments of Inertia be $I_A$, $I_B$, and $I_C$ where $I_A \leq I_B \leq I_C$. The rotational kinetic energy of the molecule can be expressed in terms of the Principal Axes as the following

$$T_r = \frac{1}{2}(I_A\omega_A^2 + I_B\omega_B^2 + I_C\omega_B^2). \tag{3.6}$$

Using the definition $J_x = \frac{\delta T}{\delta \omega_x}$ the total angular momentum about the Principal Axes are

$$J_A = I_A\omega_A \tag{3.7}$$
$$J_B = I_B\omega_B \tag{3.8}$$
$$J_C = I_C\omega_C. \tag{3.9}$$

Using Eqns.3.9 and Eqn.3.6 the Hamiltonian can be expressed in terms of the molecule's total angular momentum about its Principal axes and its Principal Moments of Inertia (diagonal elements of **I**) as the following

$$H_r = AJ_a^2 + BJ_b^2 + CJ_c^2 \tag{3.10}$$

where A,B, C are the Principal rotational constants $A = 1/(2I_A)$,$B = 1/(2I_B)$, and $C = 1/(2I_C)$. These constants terms follow the *Rigid Rotor Approximation* which simply implies that vibrational motion is negligible, and the moments of inertia remain unchanged with respect to time. The Hamiltonian in the above form (Eqn.3.10) is much more manageable than a Hamiltonian described in terms of the axes of the molecular fixed frame. Therefore, the rotational energy levels for the molecule will be much easier to determine. To determine the complete set of rotational energy levels for a molecule, all eigenvalues to the rotational Hamiltonian must be calculated (e.g. find the solution to $H_r|E_r >= E_r|E_r >$).

The next step in determining eigenvalues for the rotational Hamiltonian requires

angular momentum properties to be known. Therefore, the following angular momentum properties are presented

$$[J_i, J_i] = ie_{ijk}J_k \qquad J_\pm = J_x \pm iJ_y \tag{3.11}$$
$$[J_iJ_i, J_j] = 0 \qquad J^\pm = J_b \pm iJ_c \tag{3.12}$$

$$J^2 = J_iJ_i = J_i^2 + J_j^2 + J_k^2. \tag{3.13}$$

Note, again, that the indices follow Einstein summation notation and $i, j, k = A, B, C$ (for Principal Axes) and x,y,z (for space fixed frame). For asymmetric top molecules its convenient to rewrite $H_r$ by substituting Eqns.3.12 and 3.13 into Eqn.3.10. It can be shown that the molecule has a matrix $H_r$ of the form

$$H_r = \frac{1}{2}(A+B)J^2 + (C - \frac{1}{2}(A+B))J_C^2) + \frac{1}{4}(A-B)(J^{+2} + J^{-2}) \tag{3.14}$$

and can be represented by basis states $|JK>$ where J and K take on integer values. All matrix elements can be calculated using the equations

$$< JK|J^2|JK > = J(J+1) \tag{3.15}$$
$$< JK|J_c^2|JK > = K^2 \tag{3.16}$$

$$< JK+2|J^-J^-|JK > = < JK|J^+J^+|JK+2 > \tag{3.17}$$
$$= \sqrt{(J-K)(J+K+1)(J-K-1)(J+K+2)} \tag{3.18}$$

$$< JK-2|J^+J^+|JK > = < JK|J^-J^-|JK-2 > \tag{3.19}$$
$$= \sqrt{(J+K)(J-K+1)(J+K-1)(J-K+2)} \tag{3.20}$$

Since the rotational Hamiltonian is diagonal in **J**, it reduces to sets of matrices of differing J with dimension $(2J+1) \times (2J+1)$. For example, consider the simple case where $J = 1$ and the above relations for $H_r$'s matrix elements, the matrix $H_r$ becomes

$$H_r = \begin{bmatrix} \frac{A+B}{2} + C & 0 & \frac{A-B}{2} \\ 0 & A+B & 0 \\ \frac{A-B}{2} & 0 & \frac{A+B}{2} + C \end{bmatrix}.$$

The matrix is symmetric along both diagonals and related to the fact that the basis $|JK>$ is degenerate in $\pm K$. For asymmetric top molecules, the new basis

representation

$$\frac{1}{\sqrt{2}}|J+K> \pm |J-K> \tag{3.21}$$

is more convienent to use in conjunction with the Wang unitary transformation matrix. This is the easiest way to diagonalize the rotational Hamiltonian and find energy values for all the different available rotational transitions for asymmetric tops. Upon employing this procedure we obtain

$$H_r = \begin{bmatrix} B+C & 0 & 0 \\ 0 & A+B & 0 \\ 0 & 0 & A+C \end{bmatrix}.$$

The eigenvalues from the diagonalized Hamiltonian (equation above) correspond to the following eigenstates for the $J = 1$ rotational transition

$$E(1_{10}) = A + B \tag{3.22}$$
$$E(1_{11}) = A + C \tag{3.23}$$
$$E(1_{01}) = B + C \tag{3.24}$$

### 3.1.1 Radiative Transfer

Radiative transfer is the transfer of radiation through a medium by means of emission, absorption, and scattering from molecules and/or atoms within the medium. For molecular clouds, radiative transfer is one of the physical processes that governs the dynamics of such regions. This is because radiative transfer serves as a cooling mechanism and temperature is directly related to the speed of particles in a particular medium. For the research presented in this thesis, the radiative transfer in molecular clouds containing an intermediate mass protostar is calculated. Due to the relatively low molecular densities known to exist in these regions the effect of scattering is negligible and is excluded from the radiative transfer equation

$$\frac{dI_\nu}{d\tau_\nu} = -I_\nu + S_\nu \tag{3.25}$$

where $I_\nu$ is the intensity at frequency $\nu$, and $S_\nu$ is the source function. The above equation describes the interactions between light and the medium through which it is propogating. To describe how AMC calculates the radiative transfer (Eqn. 3.25) in molecular clouds the theory and definitions required to understand this process are presented. The source function term in the radiative transfer equation is defined as

$$S_\nu = \frac{j_\nu}{\alpha_\nu} \tag{3.26}$$

where $j_\nu$ and $\alpha_\nu$ are the emission and absorption coefficient, respectively. The emission and absorption of molecules and dust in the molecular cloud are both taken into consideration (e.g. $j_\nu = j_\nu(dust) + j_\nu(gas)$, $\alpha_\nu = \alpha_\nu(dust) + \alpha_\nu(gas)$). The components for each of the coefficients are given by

$$j_\nu(dust) = \alpha_\nu(dust) \qquad j_\nu(gas) = \frac{h\nu_o}{4\pi} n_u A_{ul} \phi(\nu) \tag{3.27}$$

$$\alpha_\nu(dust) = \kappa_\nu \rho_{dust} \qquad \alpha_\nu(gas) = \frac{h\nu_o}{4\pi}(n_l B_{lu} - n_u B_{ul})\phi_\nu \tag{3.28}$$

where the indices l and u refer to the lower and upper energy levels of a particular transition between different rotational states for the molecule of interest. The $\nu_o$ refers to the frequency at which the transition is observed and the $A_{ul}$, $B_{lu}$, and $B_{ul}$ are known as Einstein coefficients. The Einstein coefficient $A_{ul}$ represents the instantaneous emission rate of a photon by the molecule, whereas, the $B_{ul/lu}$ coefficients represent the induced emission from interactions with the local mean radiation field, $J_\nu$, given by

$$J_\nu = \frac{1}{4\pi} \int I_\nu d\omega. \tag{3.29}$$

In the above equation $\omega$ is a solid angle and $n_l$ and $n_u$ represent the number of molecules (in $cm^{-3}$) that exist in the lower or upper rotational energy level of a particular transition. For water, $A_{ul/lu}$ for each transition is known. Furthermore, $B_{ul/lu}$ can be expressed in terms of $A_{ul}$'s. Finally, the $\phi_\nu$ is the line profile function. For most molecular clouds, the predicted line profile function is given by

$$\phi_\nu = \frac{c}{b\nu_o\sqrt{\pi}} \exp -\frac{c^2(\nu - \nu_o)^2}{\nu_o^2 b^2} \tag{3.30}$$

where c is the speed of light and b is the full width of the line (km/s). All level populations for the investigated molecule are calculated by AMC through the equation of statistical equilibrium

$$n_l[\sum_{k<l} A_{lk} + \sum_{k\neq l}(B_{lk}J_\nu + C_{lk})] = \sum_{k>l} n_{k>l} A_{kl} + \sum_{k\neq l} n_k(B_{kl}J_\nu + C_{kl}). \tag{3.31}$$

In the above equation $C_{kl}$ are the collisions rates for the molecule which depend on envirnomental variables and molecular properties. To calculate the level populations the radiation field, $J_\nu$, must to be known. However, $J_\nu$ itself depends on the radiative transfer equation, Eqn. 3.25, and the absorption and emission coefficients, Eqn. 3.28. AMC uses the Monte Carlo method to iteratively converge on $J_\nu$ in every radial cell in the input model. Specifically, the program AMC starts by making an initial guess on the level populations for the molecules and calculates $J_\nu$. The statistical equilibrium equation is then solved and by Monte Carlo integration new

populations are obtained. A new value for $J_\nu$ is determined and AMC adjusts the populations again. The process continues until the radiation field and level populations converge on a consistent solution. For this research, the consistent solution is considered to have been obtained once the difference between level populations from one iteration to the next is $\leq 1 \times 10^{-6}$. This is completed for every radial cell in the input model. With the level populations for all levels known throughout the profile of the cloud the emission distribution of any rotational transition is mapped on the sky from ray tracing. RATRAN's secondary program, SKY, implements the ray tracing procedure.

# Chapter 4

# Results

In this chapter the results of this research, the modeled spectral lines of water from intermediate mass star formation regions are presented and discussed. Ten lines are selected for investigation. These ten lines are chosen because their frequencies are in the observable range of the Herschel Space Observatory using HIFI, the Heterodyne Instrument for the Far Infrared, and the excitation energies associated with these lines are within the temperature domain of our modeled regions. Details for the ten lines along with their associated HIFI beam size are listed in Table 4.1.

The water lines are modeled from star formation regions with an early stage intermediate mass protostar centrally located in a spherically symmetric static protostellar envelope at a distance of 1 kpc. The details of these regions can be found in Chapter 2. To model these water lines the program RATRAN [9] is used (see Section 2.2). As mentioned earlier, the AMC program implements the Monte Carlo method and calculates the level populations of the molecule under investigation throughout a spherical region which is supplied as input. The SKY program then uses the level populations to construct the source function at every position in the input model. To calculate the molecular emission distribution from the region the program traces all rays from every position. In addition the user supplies the velocity profile for the region. In this research, the velocity throughout the profile was set to 0 $kms^{-1}$. Furthermore, we chose to output the $H_2O$ emission distribution as a FITS image. For each line a FITS image of the emission from the modeled region was convolved to its appropriate Herschel beam size (see Table 4.1) and its spectral profile at the x,y center of the region was produced. The water lines from each model are presented in Figures 4.1-4.18.

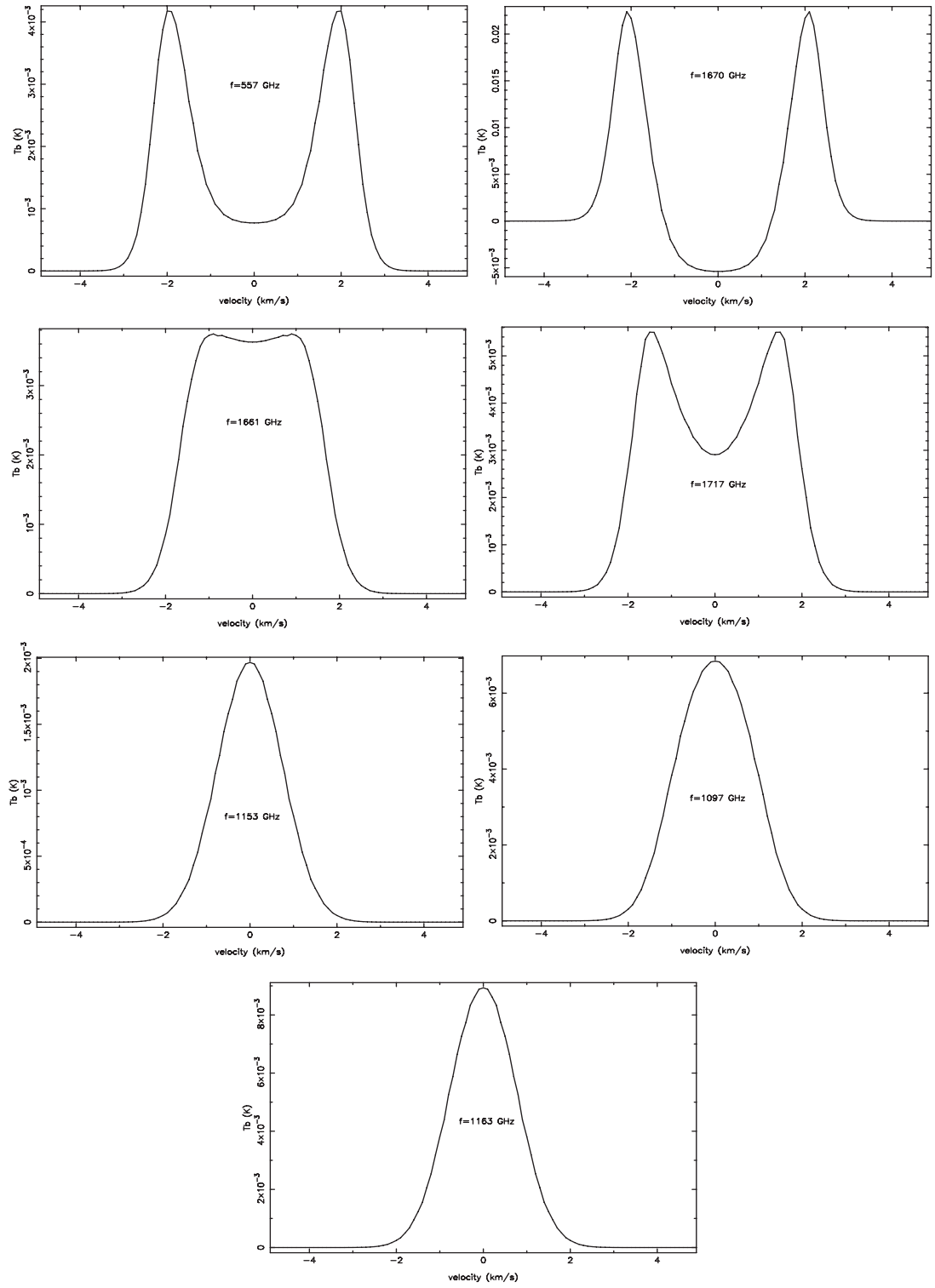


Figure 4.1: Ortho water lines for Model 1: $M_{gas} = 10M_{\odot}$, $L = 100L_{\odot}$.

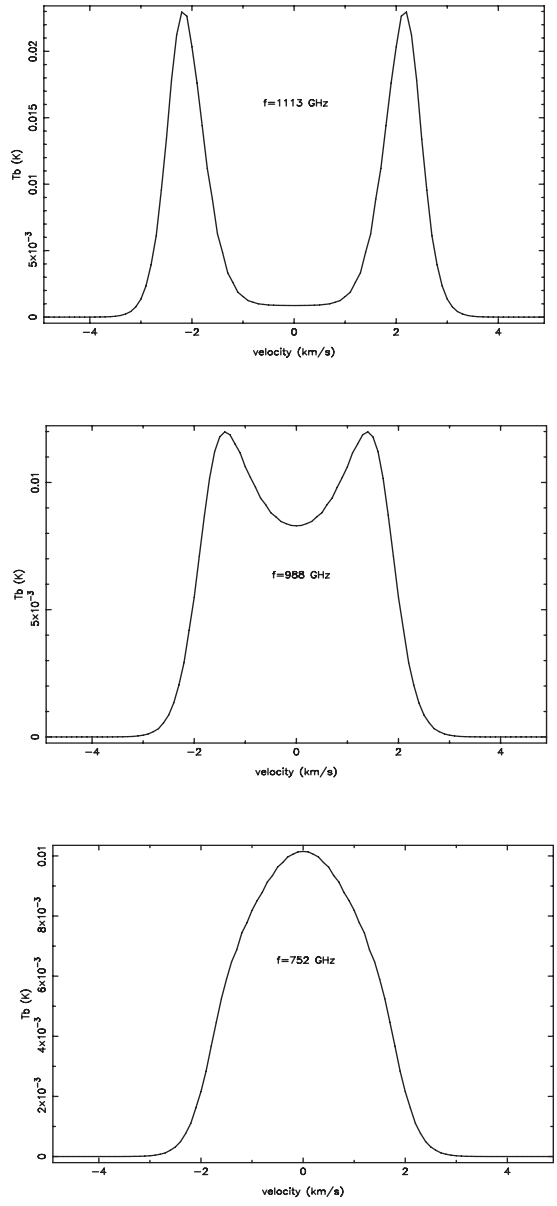


Figure 4.2: Para water lines for Model 1: $M_{gas} = 10M_{\odot}$, $L = 100L_{\odot}$.

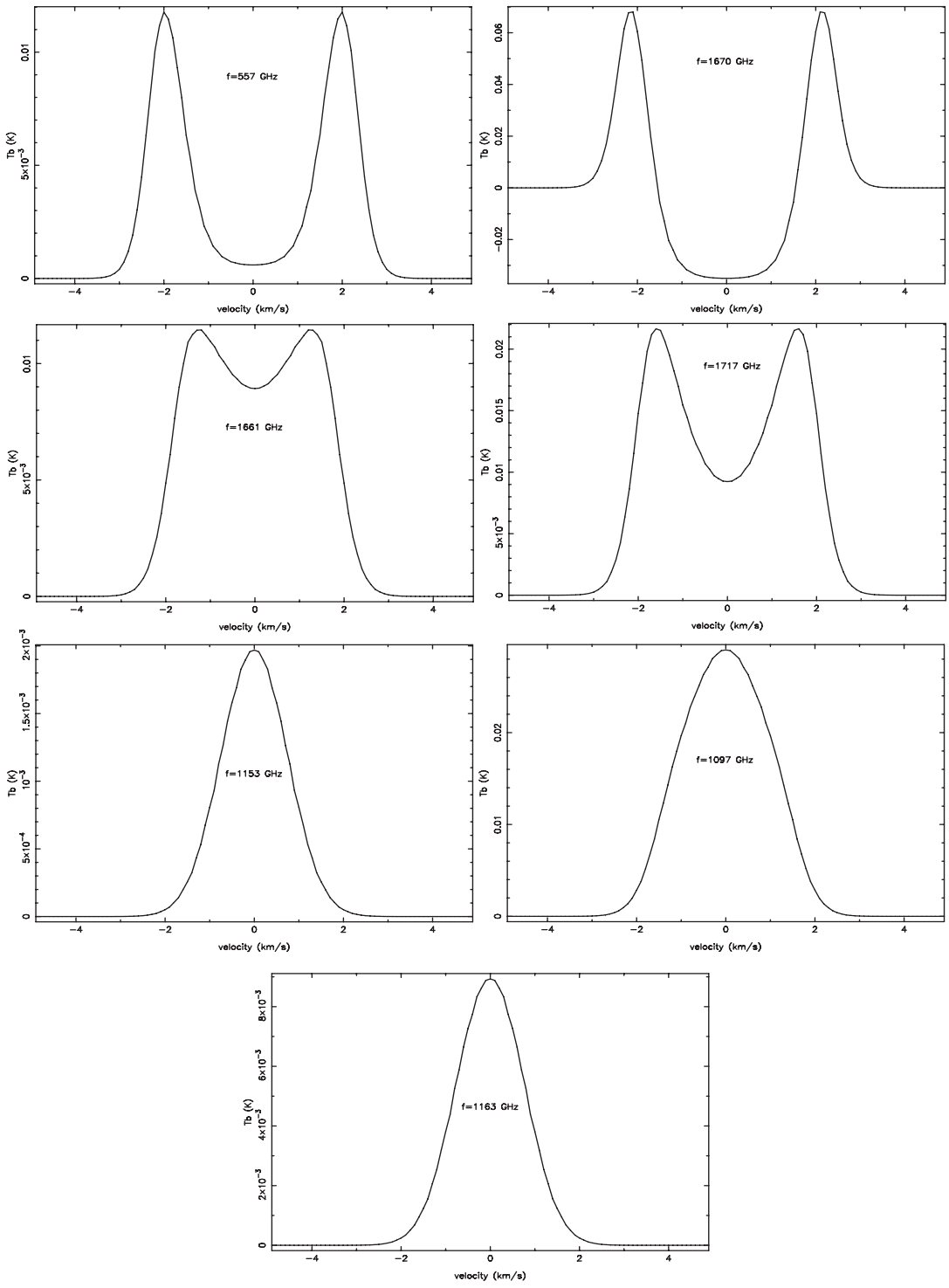


Figure 4.3: Ortho water lines for Model 2: $M_{gas} = 10M_{\odot}$, $L = 500L_{\odot}$.

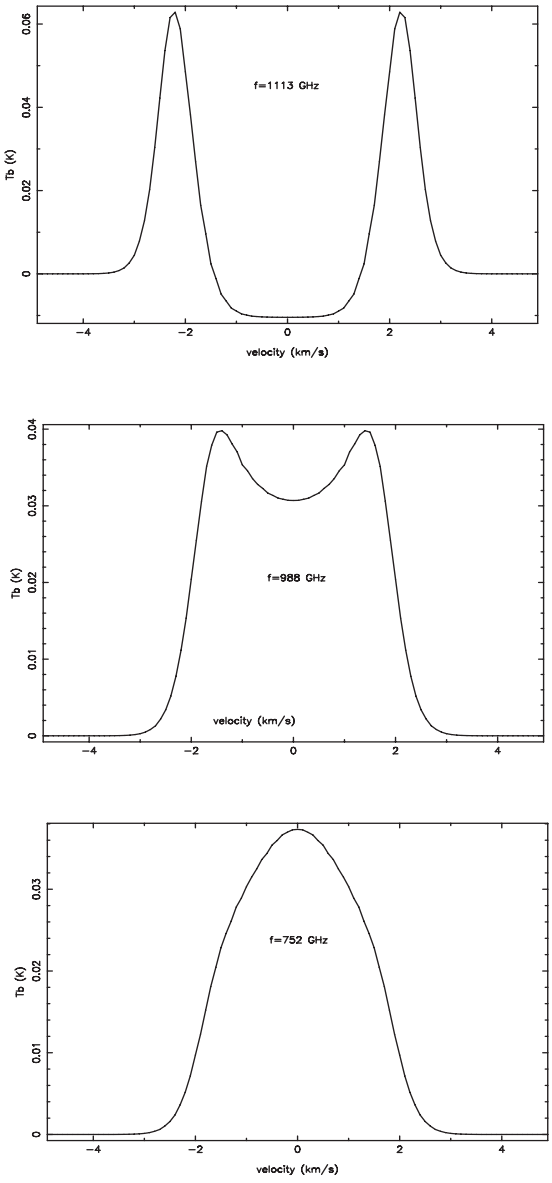


Figure 4.4: Para water lines for Model 2: $M_{gas} = 10M_{\odot}$, $L = 500L_{\odot}$.

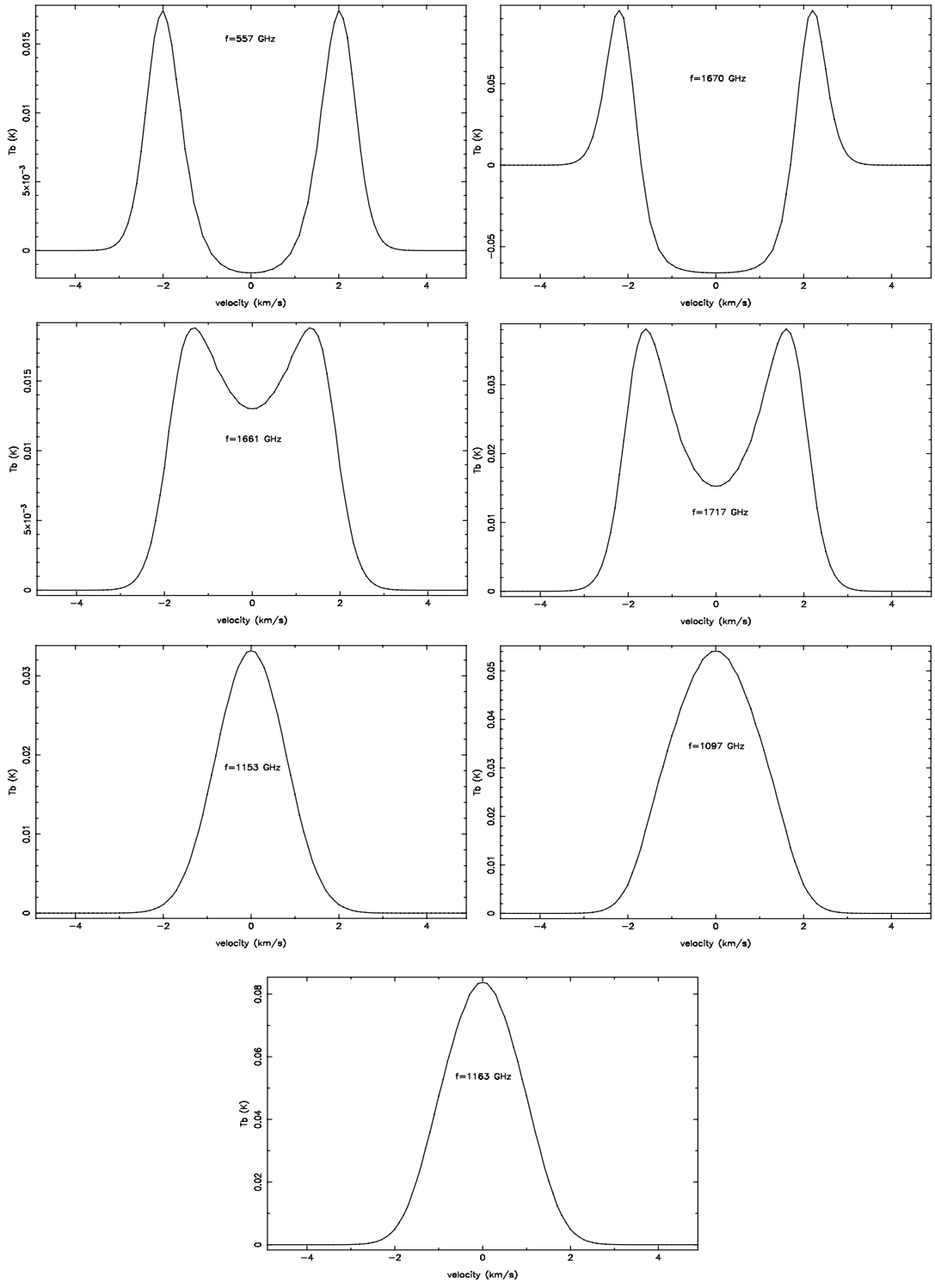


Figure 4.5: Ortho water lines for Model 3: $M_{gas} = 10M_{\odot}$, $L = 1000L_{\odot}$.

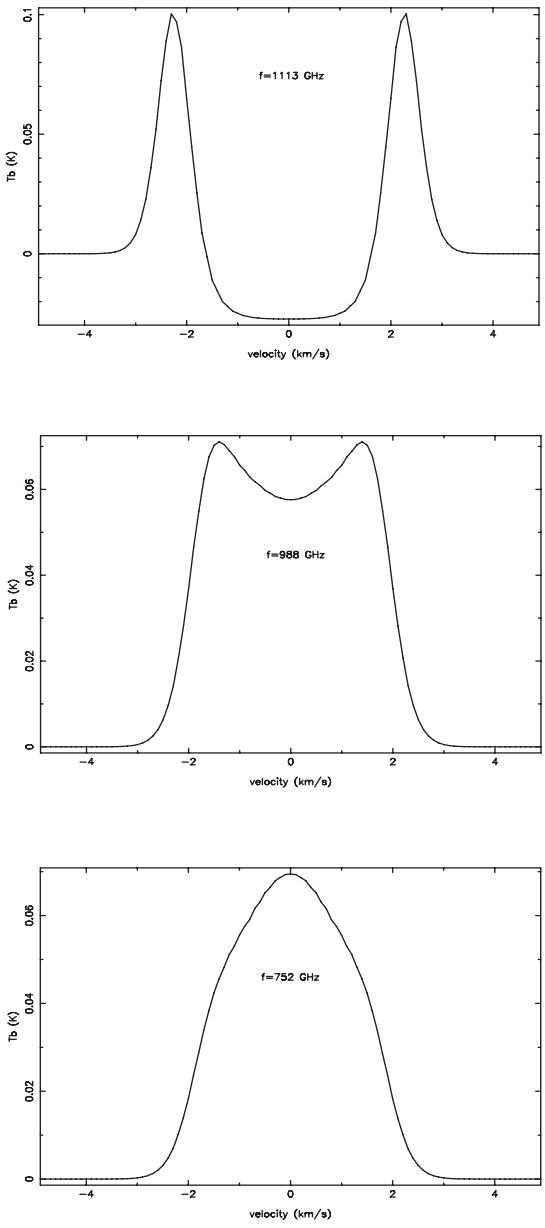


Figure 4.6: Para water lines for Model 3: $M_{gas} = 100M_{\odot}$, $L = 1000L_{\odot}$.

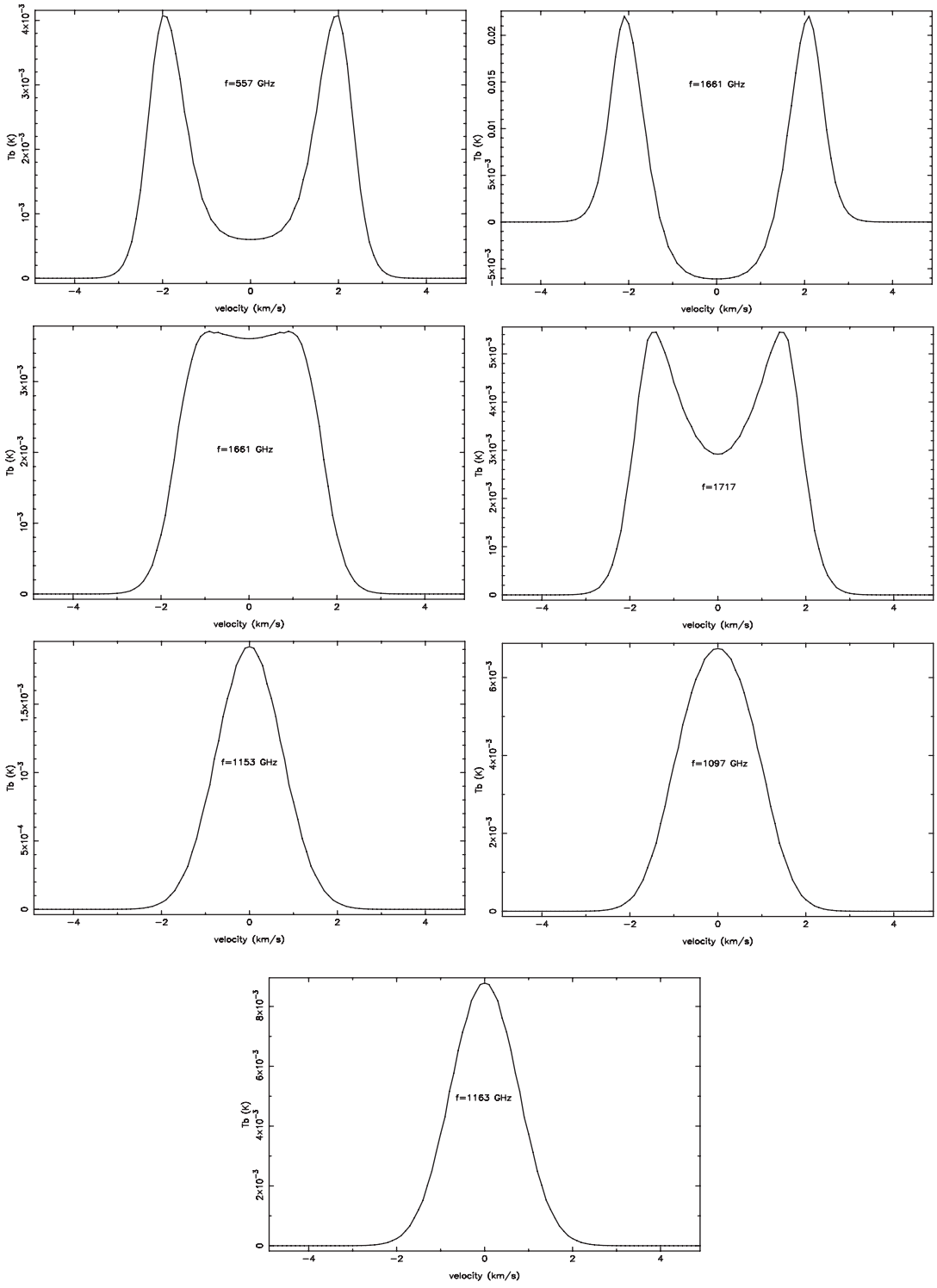


Figure 4.7: Ortho water lines for Model 4: $M_{gas} = 100M_{\odot}$, $L = 100L_{\odot}$.

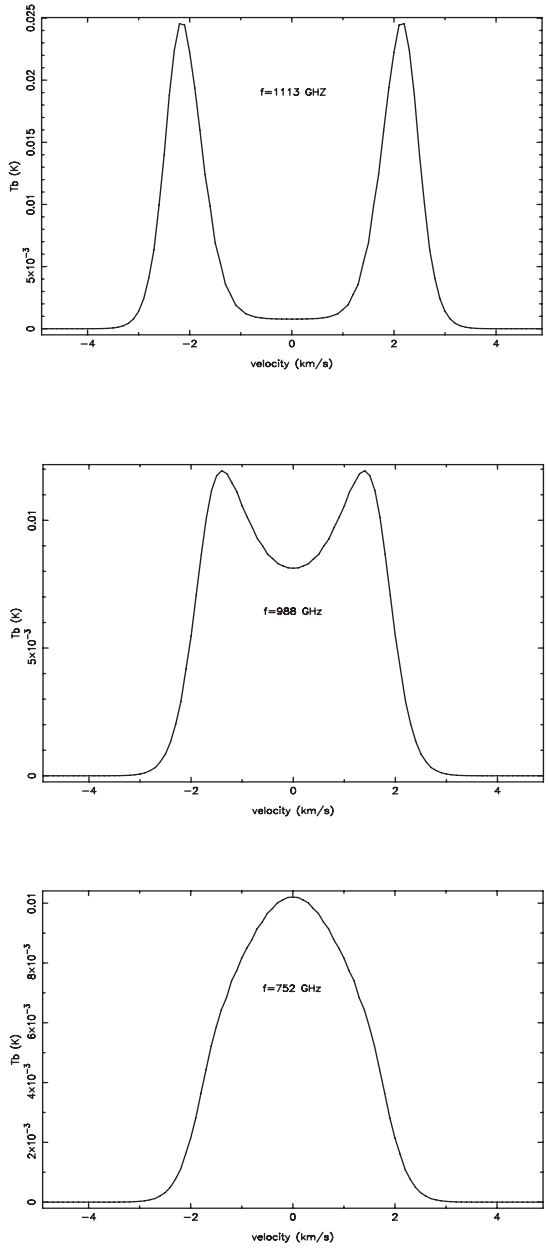


Figure 4.8: Para water lines for Model 4: $M_{gas} = 100M_{\odot}$, $L = 100L_{\odot}$.

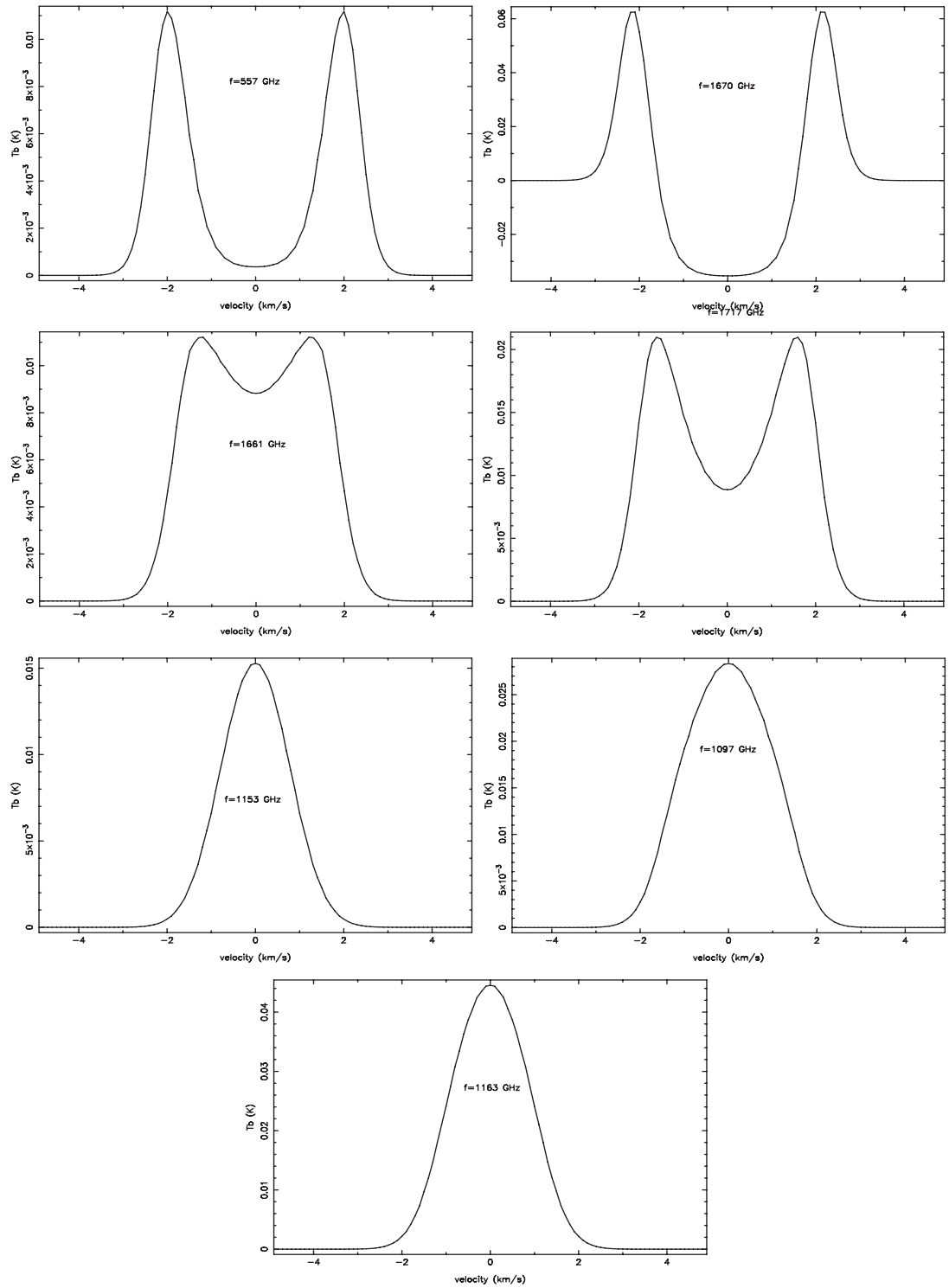


Figure 4.9: Ortho water lines for Model 5: $M_{gas} = 100M_{\odot}$, $L = 500L_{\odot}$.

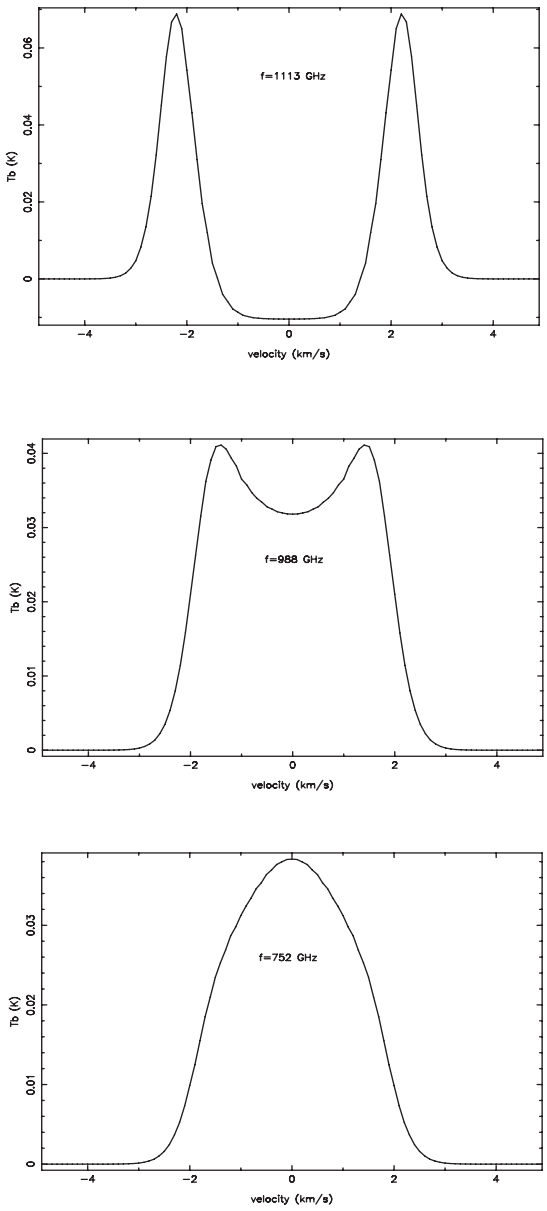


Figure 4.10: Para water lines for Model 5: $M_{gas} = 100M_{\odot}$, $L = 500L_{\odot}$.

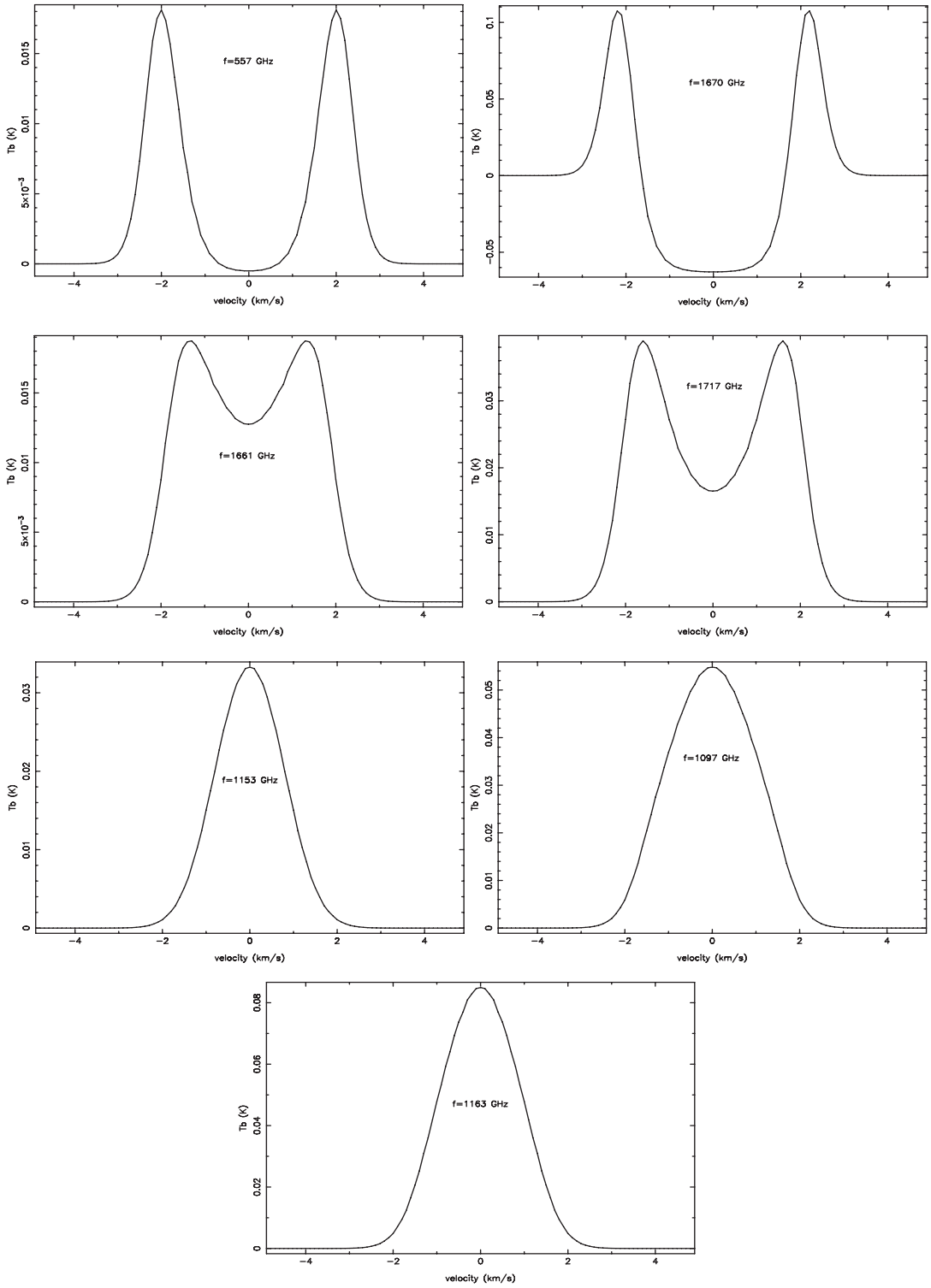


Figure 4.11: Ortho water lines for Model 6: $M_{gas} = 100M_{\odot}$, $L = 1000L_{\odot}$.

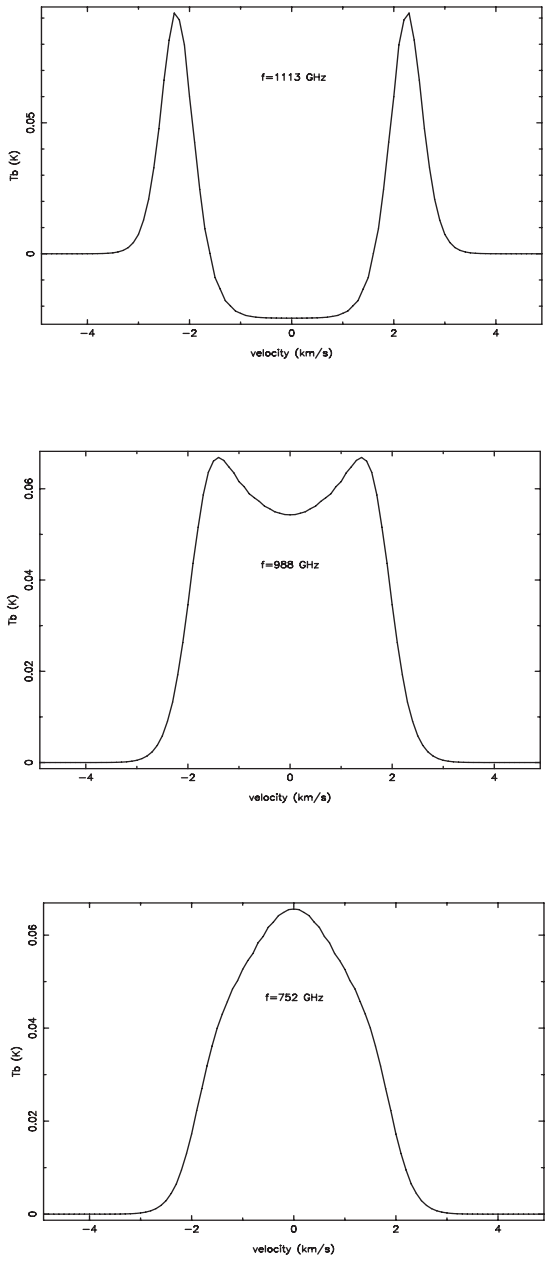


Figure 4.12: Para water lines for Model 6: $M_{gas} = 100M_{\odot}$, $L = 1000L_{\odot}$.

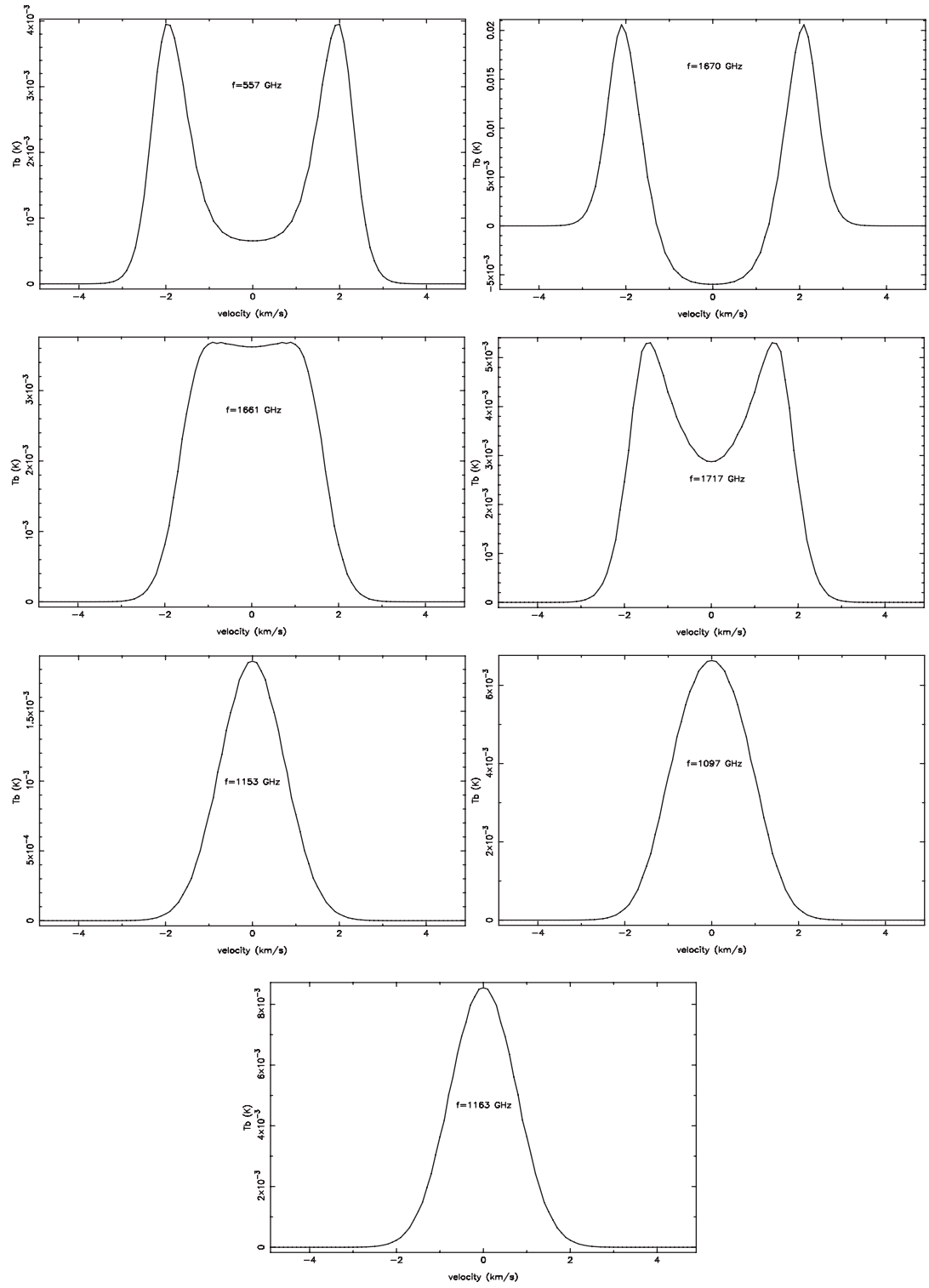


Figure 4.13: Ortho water lines for Model 7: $M_{gas} = 500M_{\odot}$, $L = 100L_{\odot}$.

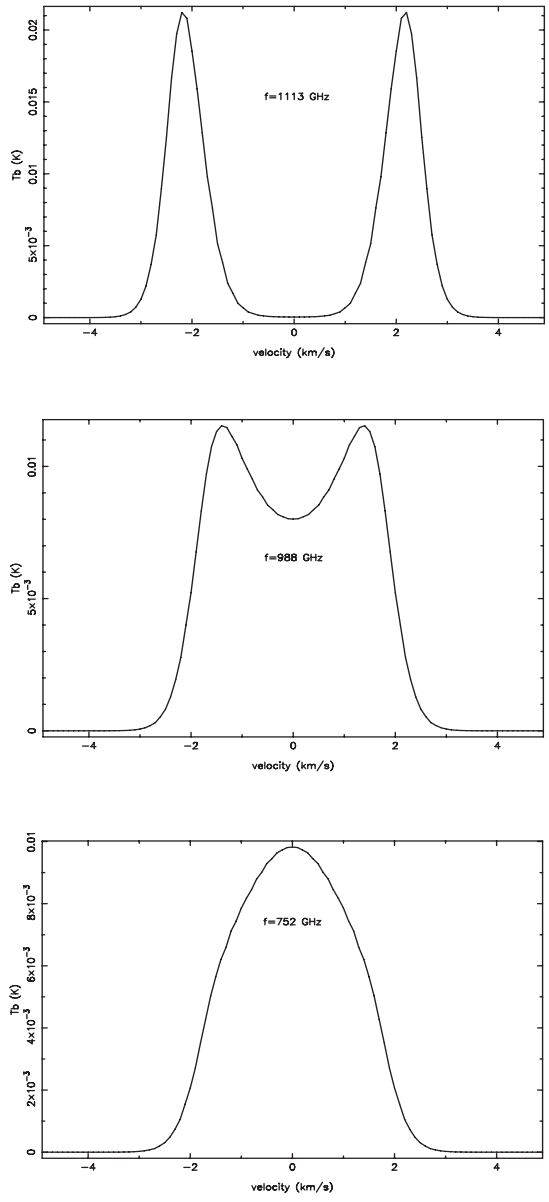


Figure 4.14: Para water lines for Model 7: $M_{gas} = 500M_{\odot}$, $L = 100L_{\odot}$.

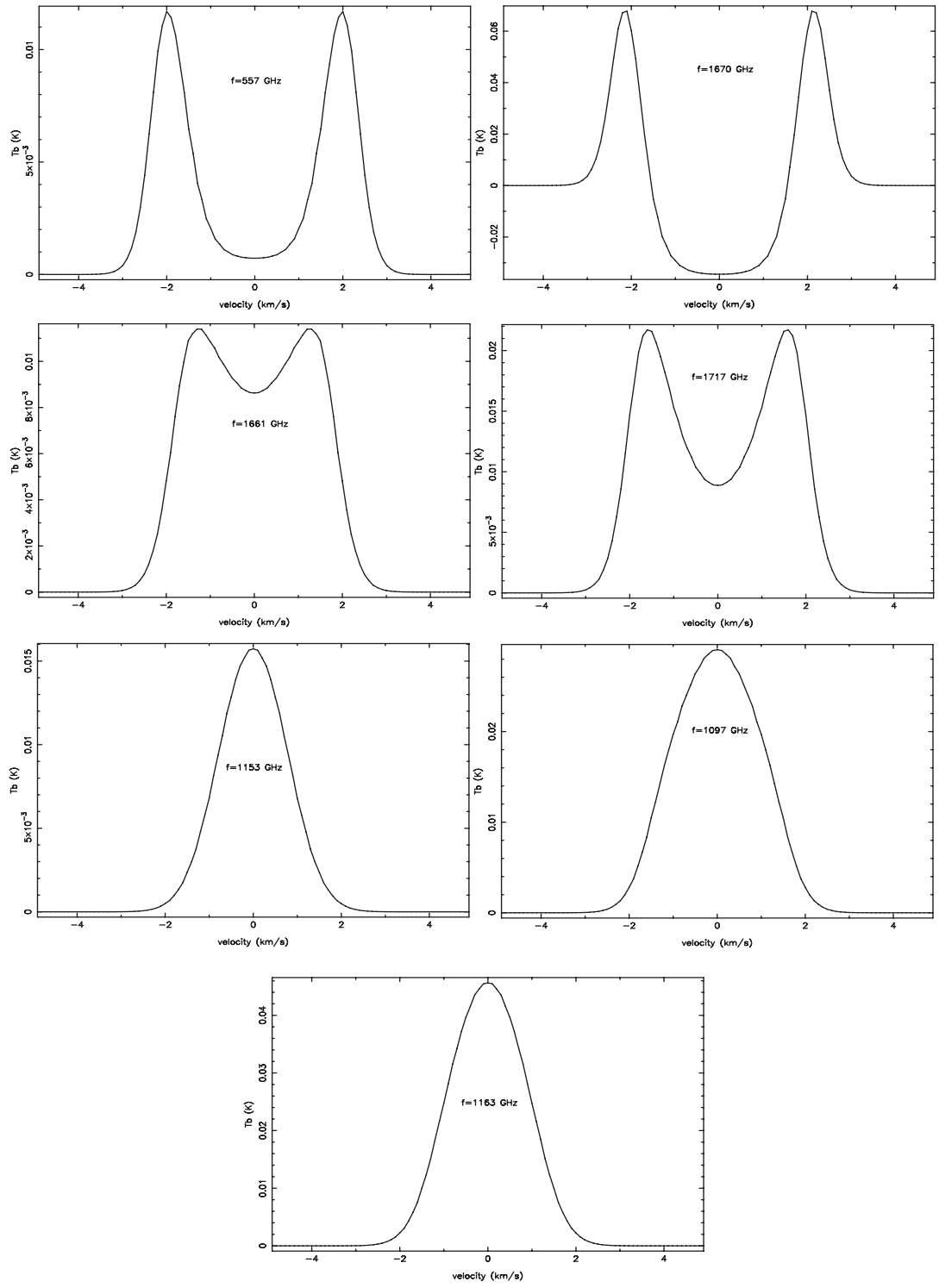


Figure 4.15: Ortho water lines for Model 7: $M_{gas} = 500M_{\odot}$, $L = 500L_{\odot}$.

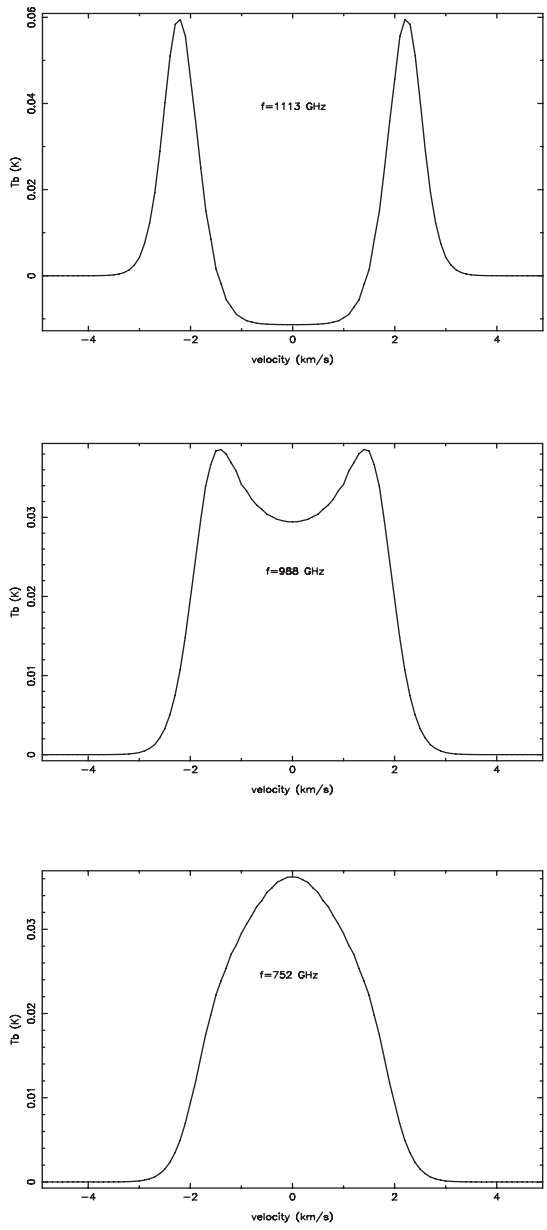


Figure 4.16: Para water lines for Model 8: $M_{gas} = 500M_{\odot}$, $L = 500L_{\odot}$.

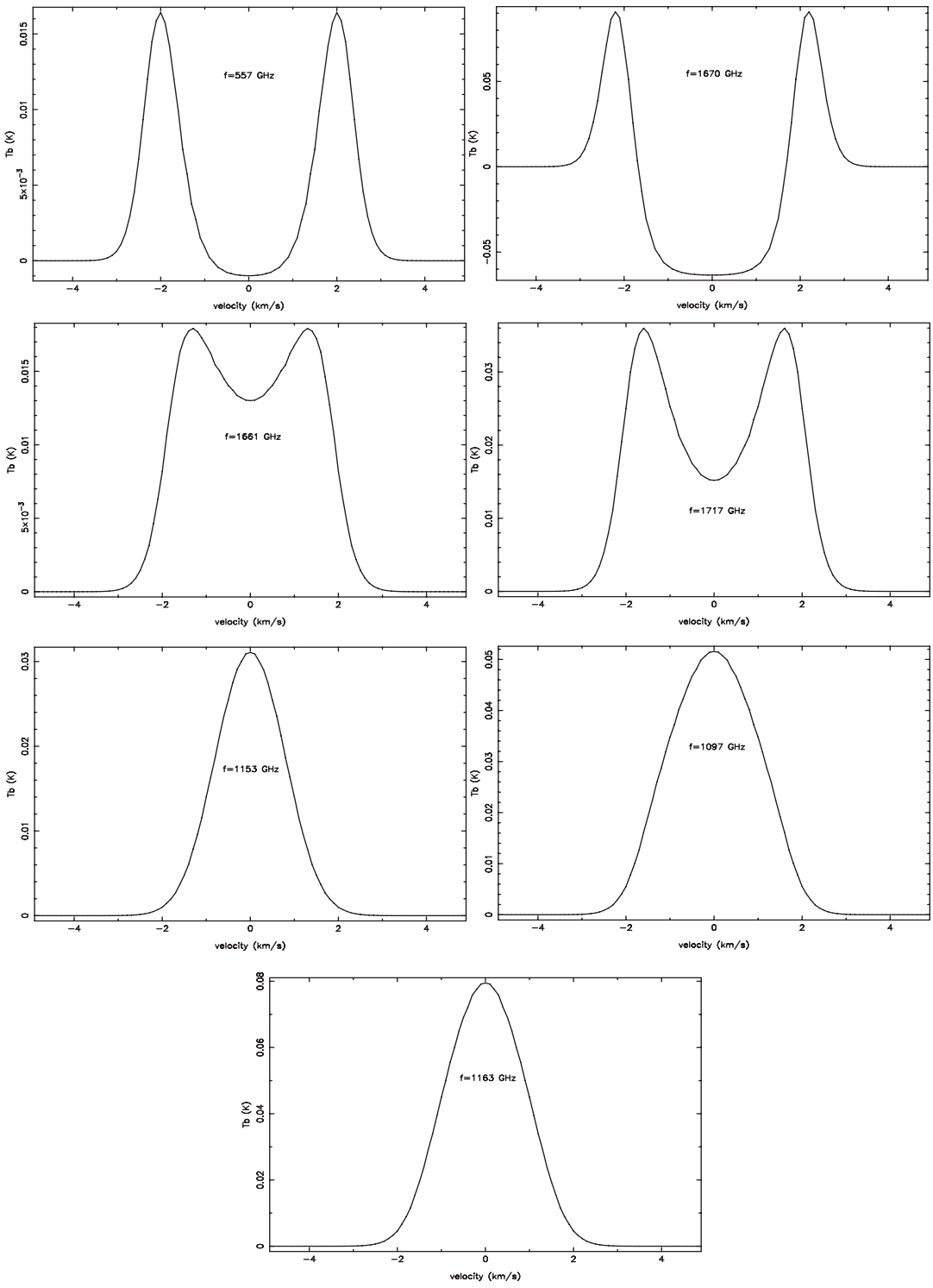


Figure 4.17: Ortho water lines for Model 9: $M_{gas} = 500M_{\odot}$, $L = 1000L_{\odot}$.

| Ortho Water Transitions | | | |
|---|---|---|---|
| Transition | Frequency (GHz) | Energy (K) | Beam size (") |
| $1_{10} - 1_{01}$ | 557 | 61.0 | 39 |
| $2_{12} - 2_{01}$ | 1670 | 114.4 | 13 |
| $2_{21} - 2_{12}$ | 1661 | 194.1 | 13 |
| $3_{03} - 2_{12}$ | 1717 | 196.8 | 13 |
| $3_{12} - 2_{21}$ | 1153 | 249.4 | 19 |
| $3_{12} - 3_{03}$ | 1097 | 249.4 | 20 |
| $3_{21} - 3_{12}$ | 1163 | 305.3 | 19 |
| Para Water Transitions | | | |
| $1_{11} - 0_{00}$ | 1113 | 53.4 | 19 |
| $2_{02} - 1_{11}$ | 988 | 100.8 | 22 |
| $2_{11} - 2_{02}$ | 752 | 136.9 | 29 |

Table 4.1: Herschel's observable water lines from intermediate mass star formation regions.

As mentioned in Chapter 2, the nine models are described by the protostar's luminosity and the mass contained in the protostellar envelope. The analysis of water lines gives environmental information for the region from which they originate. In this research, our analysis of water lines from our modeled star formation regions allows us to associate particular lines and sets of lines to probe the source's luminosity and its surrounding envelope mass. First, a summary of the important features notes on our modeled water lines is presented.

## 4.1 Line strengths

The line strengths of all of our lines are in terms of antenna temperatures (units are in K) and are very weak in comparison to similiar studies [17,20,21]. However, this is the first study completed on water lines from intermediate mass star formation regions. The origin of these weak lines strengths is a result of the particular regions which are modeled. For the low mass star formation region study of van Kempen, their star formation regions are modeled at a distance of 150 pc since many candidate low mass objects are at this distance. Their line strengths for optically thick and thin lines are two orders of magitude stronger than ours due to both distance and beam dilution. The flux, $F_\nu$, is $F_\nu \propto r^{-2}$ and the beam dilution, $b_{dilution}$, is $b_{dilution} \propto A_{source(\tau \approx 2/3)}/A_{beam}$ (where A which is $\propto r^2$ is the area). Since our modeled regions are at a distance of 1 kpc the beam is much larger than the emitting area on the sky weak line strengths are obtained. In comparision to the [17] study of water lines from high mass star formation regions, our line strengths are again two orders of magnitude weaker. In this case, however, their regions are placed at a distance of 1 kpc, the same as ours. But, for high mass star formation regions

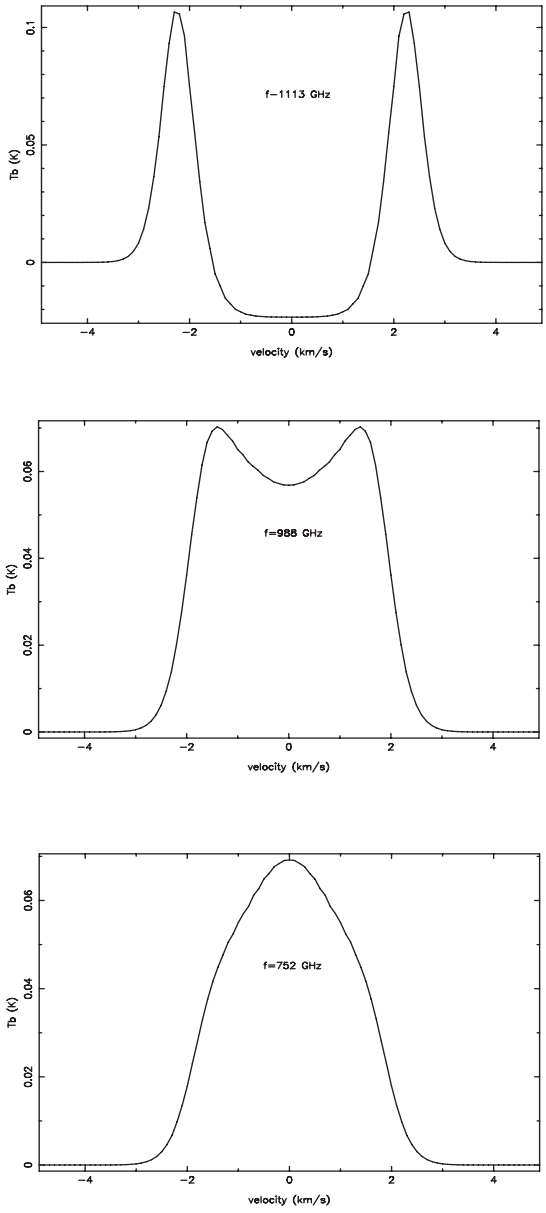


Figure 4.18: Para water lines for Model 9: $M_{gas} = 500M_{\odot}$, $L = 1000L_{\odot}$.

the source luminosities that are associated with its protostar are much higher than for intermediate mass protostars. Their line profiles suffer from beam dilution as well but since the luminosities are much higher they get much brighter emission. The effect of distance on the line strengths is illustrated in Fig 4.19. where the lines $1_{10} - 1_{01}$ and $3_{21} - 3_{12}$ are modeled from the same region but its distance is varied from 100 pc to 1000 pc. Very large differences are observed; closer regions have much stronger line strengths.

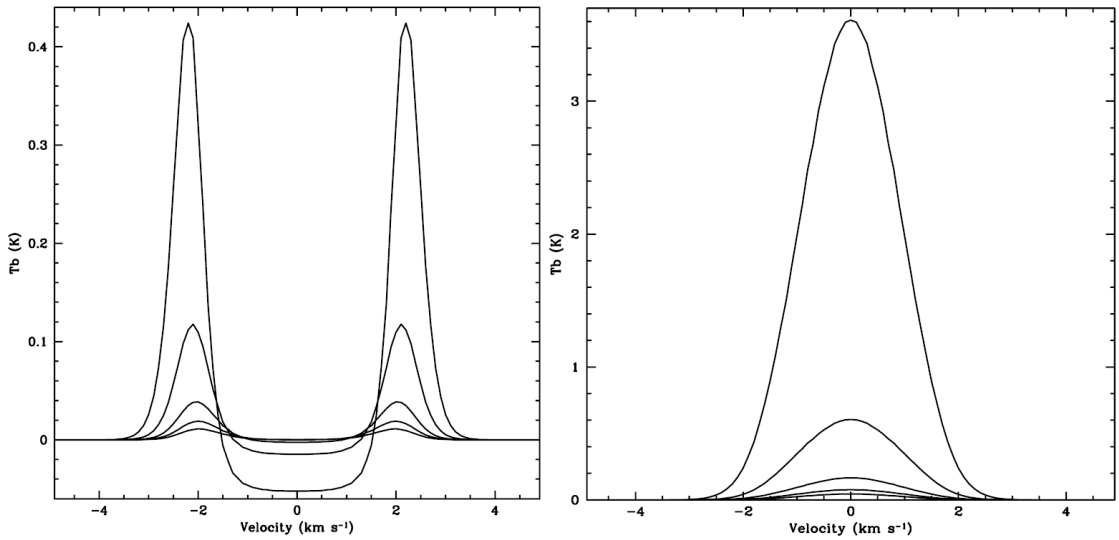


Figure 4.19: The effect of distance on the $1_{10} - 1_{01}$ and $3_{21} - 3_{12}$ lines modeled from Model 5 ($M_{env} = 100 M_{\odot}$, $L = 500 L_{\odot}$. Lines at distances of 100, 250, 500, 750, 1000 pc computed. Stronger line strengths are from closer regions.

The integration times required to detected such weak line strengths at distances of 1 kpc or greater would be too long for most lines, especially for the optically thick lines. In particular, the optically thick lines originate from just inside the water freezeout zone that corresponds to the outermost regions of the envelopes where the density of water is very low. For the optically thin lines, most should be observable with reasonable integration times.

There are two lines that are relatively very strong in comparison to the other lines that were modeled. These lines are the optically thick line $2_{12} - 2_{01}$ and the optically thin line $3_{21} - 3_{12}$. The optically thick line reaches line strengths up to 0.1 K and the optically thin line reaches line strengths up to 0.2 K. A plot of their $T_{MB}$'s, take at the center of the line profiles, for all 9 models is show in Figure 4.20. It is illustrated on the plot that these two lines are strong luminosity probes but very poor indicators of mass.

For models of low luminosity and low envelope mass, line strengths are all below the sensitivity limit of Herschel. However, observations of water lines taken from intermediate mass star formation regions at a distance of 1 pc that yield no water

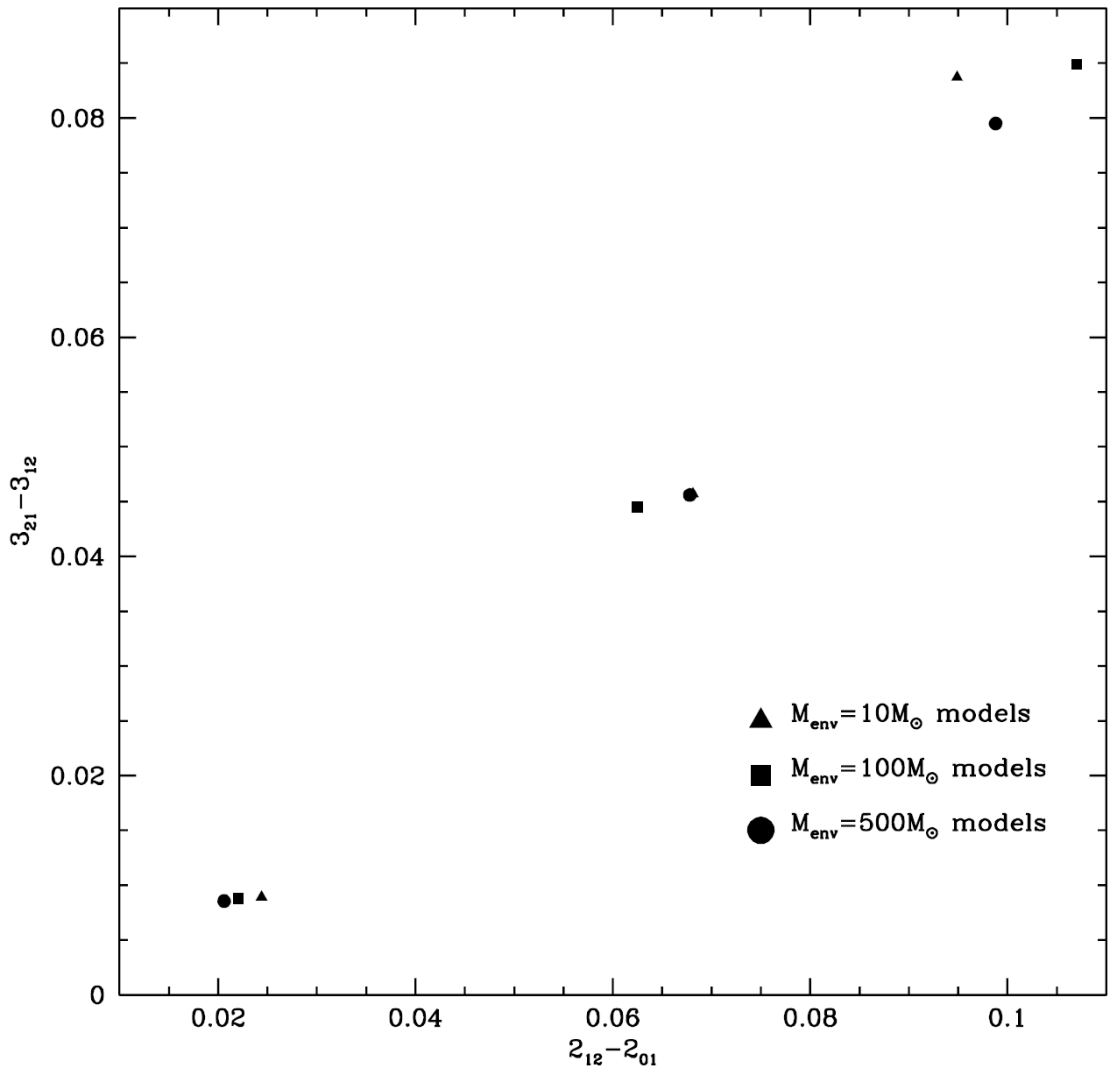


Figure 4.20: Line strengths taken at the center of the line for the two strongest lines. $3_{21}-3_{12}$ is an optically thin, high excitation line, and $2_{12}-2_{01}$ is an optically thick, low excitation line. Symbols (circle,square, and triangle) that have the same $3_{21}-3_{12}$ line strength have the same luminosity. Each grouping represents models that have the same source luminosity and different envelope mass. No correlations are found between cases of the same luminosity and different envelope mass and differences are attributed to numerical effects from the AMC code. Lines are a very strong luminosity indicator, but a very poor envelope mass indicator.

emission are suggestive that the region has both, low luminosity and low envelope mass. However, the line $2_{12} - 2_{12}$ has an interesting feature for models having low luminosities ($100L_{\odot}$). In all of our models with source luminosites of $100L_{\odot}$, the line center has a flat top profile and indicates that there is not as much water in the cooler regions in comparison to models having a higher source luminosity.

## 4.2 Line Profiles

Of the 10 modeled water lines, 6 are optically thick and 4 are optically thin. Optically thick lines are indicated by a self-absorption feature at the center of the line and have double emission peaks. The amount of self-absorption depends on how much water is absorbing the radiation originating from the inner envelope at the location where $\tau \approx 2/3$ for a given frequency. For models with the same envelope mass the self absorption is stronger with increasing luminosity.

### 4.2.1 Diagnostic lines

Line ratios are chosen as the best diagnostic tool for determining the protostar's source luminosity. The ratios of the lines are taken at the center of the line. A compilation of line ratios are tabulated in Tables 4 (for optically thick lines) and Table 5 (for optically thin lines). The best line ratios to probe luminosity are the optically thin lines. The optically thin line ratios $(3_{12} - 3_{03})/(3_{12} - 2_{21})$ and $(3_{21} - 3_{12})/(3_{12} - 2_{21})$ are most sensitive to changes in luminosity (see Table 3). In all 9 models, the ratios remain the same for models with the same source luminosity. Furthermore, these line ratios show consistent trends and decrease with increasing luminosity. The spectral resolution required to differentiate between sources with luminosities of 100 $L_{\odot}$ and 500 $L_{\odot}$ is relatively high in comparison to the resolution required to dissociate between sources with 500 $L_{\odot}$ and 1000 $L_{\odot}$. As secondary choices, the line ratios $(2_{21} - 2_{12})/(2_{12} - 2_{01})$, $(3_{03} - 2_{12})/(2_{12} - 2_{01})$, and $(3_{03} - 2_{12})/(2_{21} - 2_{12})$ are good indicators of source luminosity and exhibit consistent trends. The difficulty encountered with most of these line ratios is that spectral sensitivities of 0.0001 K are required at objects at a distance of 1 kpc. This is much too weak for reasonable integration times with Herschel/HIFI. Therefore, these line ratios can only be used for luminosity indicators for sources that are at distances on the order of 100 pc. Furthermore, integrated line intensities (see Table 2) show consistent trends but again require long integration times.

Unfortunately, there are no key diagnostic lines in our analysis that probe the envelope masses from our analysis. This is due to the fact that line strengths, line ratios, ratios of peak to absorption intensities of optically thick lines, and integrated line intensities do not show any consistent trends with increasing or decreasing envelope masses. This is also illustrated for the two strongest lines plot (Figure 4.20). The plot of level populations of water molecules as a function of radius

| Integrated Intensities $\int T_{MB} dV$ $[Kkms^{-1}]$ | | | | | | | | | | |
|---|---|---|---|---|---|---|---|---|---|---|
| | Transition | | | | | | | | | |
| Model | $1_{10}$-$1_{01}$ | $2_{12}$-$2_{01}$ | $2_{21}$-$2_{12}$ | $3_{03}$-$2_{12}$ | $3_{12}$-$2_{21}$ | $3_{12}$-$3_{03}$ | $3_{21}$-$3_{12}$ | $1_{11}$-$0_{00}$ | $2_{02}$-$1_{11}$ | $2_{11}$-$2_{02}$ |
| Model 1 | 0.011 | 0.029 | 0.013 | 0.018 | 0.0037 | 0.015 | 0.017 | 0.045 | 0.042 | 0.031 |
| Model 2 | 0.026 | 0.016 | 0.041 | 0.070 | 0.031 | 0.074 | 0.10 | 0.075 | 0.15 | 0.12 |
| Model 3 | 0.031 | -0.054 | 0.067 | 0.12 | 0.065 | 0.14 | 0.19 | 0.072 | 0.27 | 0.22 |
| Model 4 | 0.010 | 0.026 | 0.013 | 0.018 | 0.0036 | 0.015 | 0.017 | 0.048 | 0.042 | 0.031 |
| Model 5 | 0.024 | 0.0048 | 0.041 | 0.068 | 0.030 | 0.072 | 0.097 | 0.086 | 0.15 | 0.12 |
| Model 6 | 0.035 | -0.018 | 0.066 | 0.127 | 0.065 | 0.14 | 0.19 | 0.068 | 0.25 | 0.21 |
| Model 7 | 0.010 | 0.023 | 0.013 | 0.017 | 0.0035 | 0.015 | 0.016 | 0.039 | 0.040 | 0.030 |
| Model 8 | 0.026 | 0.017 | 0.041 | 0.069 | 0.031 | 0.074 | 0.10 | 0.067 | 0.14 | 0.11 |
| Model 9 | 0.031 | -0.049 | 0.064 | 0.117 | 0.061 | 0.13 | 0.18 | 0.10 | 0.27 | 0.22 |

Table 4.2: Integrated intensities for observable $H_2O$ lines by Herschel.

for models with the same source luminosity but different envelope mass shows the origin of this behaviour, as shown in Figure 4.21. Level population profiles are exactly the same for these models. This is due to the fact that for the models of varying envelope mass their density profiles are very similiar. For high envelope mass (e.g. $M_{env} = 500 M_{\odot}$ the outer radius of the envelopes is largely increased in comparison to models with low envelope mass. The normalization of the density is set by the optical depth, the dust opacity at $100 \mu m$, and the inner radius of the envelope. It is believed that models in which the normalizations of density are separated by an order of magnitude and source luminosites that are constant would produce water lines that show consistent trends. Furthermore, water lines should have the potential to probe density. It is stressed, however, that envelope masses can still be determined by comparing observed line ratios of optically thick lines taken at $0 kms^{-1}$ and their ratio's of $T_{MB(peak)}/T_{MB(absorption)}$ with our ratios tabulated in Tables 4.3 and 4.4. For our models these ratios change significantly with mass, but dont show consistent trends. If these line ratios match with the water line observations than they suggest that region has an envelope mass that is associated with that line ratio. The more line ratios that match the greater the evidence that the regions has a envelope mass that corresponds to those line ratios.

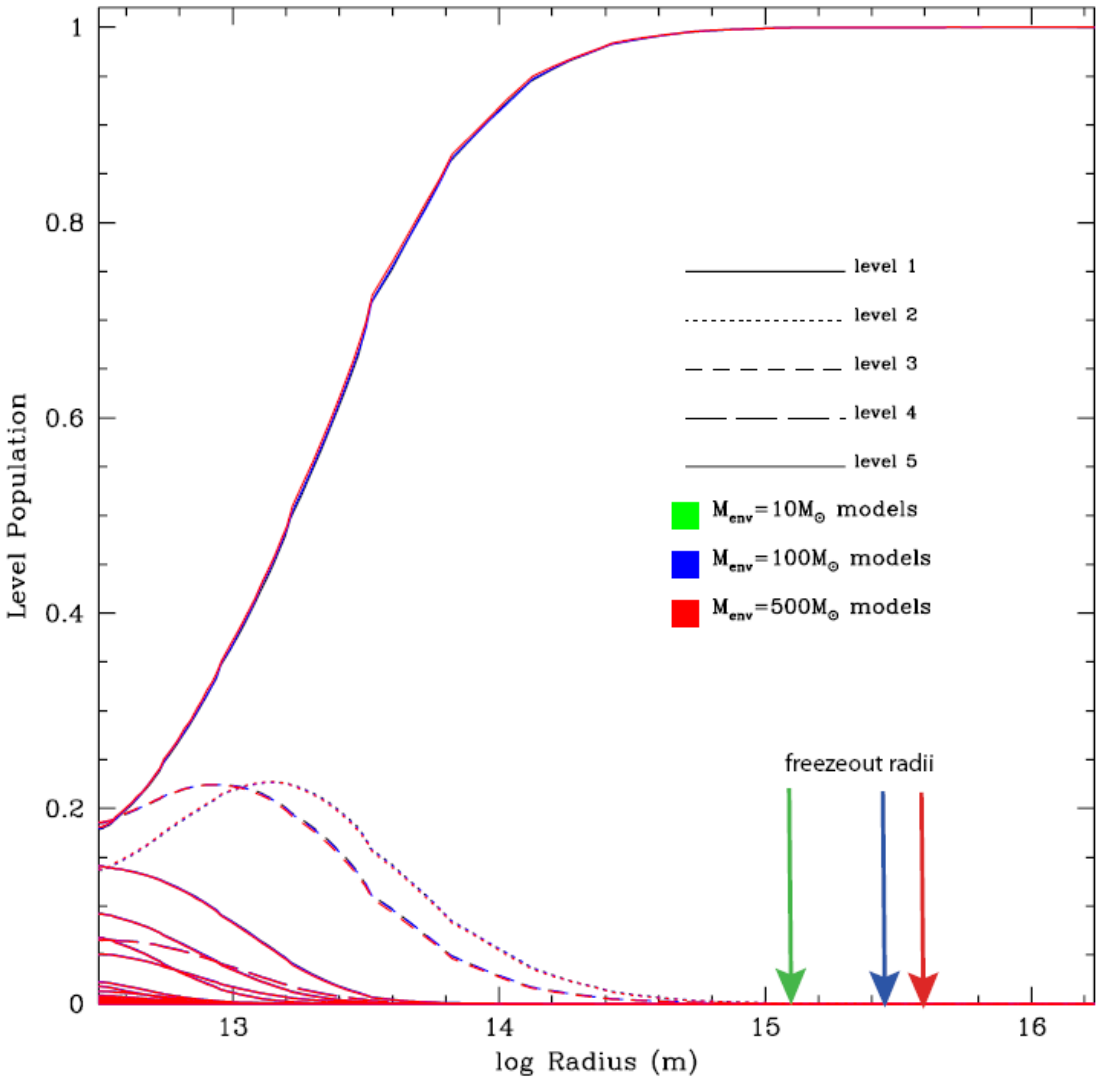


Figure 4.21: Level populations of $H_2O$ as a function of radius in the protostellar envelopes with varying masses and same source luminosity ($100L_\odot$). Level populations are the same. Coloured arrows represent freezeout radii for the models (green represent $100L_\odot$ sources, blue represent $500L_\odot$ sources, and red represent $1000L_\odot$ sources). Freezeout radius dependent on the luminosity of the source.

| $T_{MB(peak)}/T_{MB(absorption)}$ for Optically Thick Lines | | | | | | |
|---|---|---|---|---|---|---|
| Model | $1_{10}$-$1_{01}$ | $2_{12}$-$2_{01}$ | $2_{21}$-$2_{12}$ | $3_{03}$-$2_{12}$ | $1_{11}$-$0_{00}$ | $2_{02}$-$1_{11}$ |
| Model 1 (10 $M_{env} = 10M_{\odot}$, $L = 100L_{\odot}$) | 5.41 | -4.16 | 1.02 | 1.89 | 26.4 | 1.45 |
| Model 2 (10 $M_{env} = 10M_{\odot}$, $L = 500L_{\odot}$) | 19.8 | -1.95 | 1.61 | 2.35 | -6.04 | 1.30 |
| Model 3 (10 $M_{env} = 10M_{\odot}$, $L = 1000L_{\odot}$) | -10.7 | -1.44 | 1.45 | 2.49 | -3.66 | 1.23 |
| Model 4 (100 $M_{env} = 100M_{\odot}$, $L = 100L_{\odot}$) | 6.77 | -3.61 | 1.03 | 1.87 | 31.5 | 1.47 |
| Model 5 (100 $M_{env} = 100M_{\odot}$, $L = 500L_{\odot}$) | 30.8 | -1.77 | 1.27 | 2.37 | -6.62 | 1.29 |
| Model 6 (100 $M_{env} = 100M_{\odot}$, $L = 1000L_{\odot}$) | -36.1 | -1.70 | 1.46 | 2.30 | -3.74 | 1.23 |
| Model 7 (500 $M_{env} = 500M_{\odot}$, $L = 100L_{\odot}$) | 6.04 | -3.45 | 1.02 | 1.85 | 529 | 1.44 |
| Model 8 (500 $M_{env} = 500M_{\odot}$, $L = 500L_{\odot}$) | 16.2 | -1.97 | 1.32 | 2.45 | -5.22 | 1.31 |
| Model 9 (500 $M_{env} = 500M_{\odot}$, $L = 1000L_{\odot}$) | -16.6 | -1.56 | 1.38 | 2.37 | -4.59 | 1.24 |

Table 4.3: $T_{MB(peak)}/T_{MB(absorption)}$ for Optically Thick Lines

| Line Ratios for Optically Thick Lines (Center of line) | | | | | | | |
|---|---|---|---|---|---|---|---|
| Model | $\frac{2_{12}-2_{01}}{1_{10}-1_{01}}$ | $\frac{2_{21}-2_{12}}{1_{10}-1_{01}}$ | $\frac{3_{03}-2_{12}}{1_{10}-1_{01}}$ | $\frac{2_{21}-2_{12}}{2_{12}-2_{01}}$ | $\frac{3_{03}-2_{12}}{2_{12}-2_{01}}$ | $\frac{3_{03}-2_{12}}{2_{21}-2_{12}}$ | $\frac{2_{02}-1_{11}}{1_{11}-0_{00}}$ |
| Model 1 (10 $M_{env} = 10M_{\odot}$, $L = 100L_{\odot}$) | -6.98 | 4.7 | 3.77 | -0.67 | -0.54 | 0.80 | 9.54 |
| Model 2 (10 $M_{env} = 10M_{\odot}$, $L = 500L_{\odot}$) | -58.7 | 15.0 | 15.5 | -0.26 | -0.26 | 1.03 | -2.95 |
| Model 3 (10 $M_{env} = 10M_{\odot}$, $L = 1000L_{\odot}$) | 40.8 | -8.02 | -9.44 | -0.20 | -0.23 | 1.18 | -2.11 |
| Model 4 (100 $M_{env} = 100M_{\odot}$, $L = 100L_{\odot}$) | -10.1 | 6.01 | 4.86 | -0.59 | -0.48 | 0.81 | 10.5 |
| Model 5 (100 $M_{env} = 100M_{\odot}$, $L = 500L_{\odot}$) | -97.3 | 24.3 | 24.3 | -0.25 | -0.25 | 1.00 | -3.06 |
| Model 6 (100 $M_{env} = 100M_{\odot}$, $L = 1000L_{\odot}$) | 125 | -25.5 | -32.9 | -0.20 | -0.26 | 1.29 | -2.21 |
| Model 7 (500 $M_{env} = 500M_{\odot}$, $L = 100L_{\odot}$) | -9.33 | 5.54 | 4.39 | -0.61 | -0.48 | 0.79 | 200 |
| Model 8 (500 $M_{env} = 500M_{\odot}$, $L = 500L_{\odot}$) | -47.7 | 11.9 | 12.3 | -0.25 | -0.26 | 1.03 | -2.61 |
| Model 9 (500 $M_{env} = 500M_{\odot}$, $L = 1000L_{\odot}$) | 64.3 | -13.2 | -15.4 | -0.20 | -0.24 | 1.17 | -2.44 |

Table 4.4: Line Ratios for Optically Thick Lines taken from the center of line

| Line Ratios for Optically Thin Lines | | | |
|---|---|---|---|
| Model | $\frac{3_{12}-3_{03}}{3_{12}-2_{21}}$ | $\frac{3_{21}-3_{12}}{3_{12}-2_{21}}$ | $\frac{3_{21}-3_{12}}{3_{12}-3_{03}}$ |
| Model 1 (10 $M_{env} = 10M_{\odot}$, $L = 100L_{\odot}$) | 3.47 | 4.53 | 1.31 |
| Model 2 (10 $M_{env} = 10M_{\odot}$, $L = 500L_{\odot}$) | 1.82 | 2.87 | 1.58 |
| Model 3 (10 $M_{env} = 10M_{\odot}$, $L = 1000L_{\odot}$) | 1.63 | 2.52 | 1.55 |
| Model 4 (100 $M_{env} = 100M_{\odot}$, $L = 100L_{\odot}$) | 3.51 | 4.57 | 1.30 |
| Model 5 (100 $M_{env} = 100M_{\odot}$, $L = 500L_{\odot}$) | 1.85 | 2.91 | 1.57 |
| Model 6 (100 $M_{env} = 100M_{\odot}$, $L = 1000L_{\odot}$) | 1.65 | 2.55 | 1.55 |
| Model 7 (500 $M_{env} = 500M_{\odot}$, $L = 100L_{\odot}$) | 3.56 | 4.60 | 1.29 |
| Model 8 (500 $M_{env} = 500M_{\odot}$, $L = 500L_{\odot}$) | 1.85 | 2.90 | 1.57 |
| Model 9 (500 $M_{env} = 500M_{\odot}$, $L = 1000L_{\odot}$) | 1.66 | 2.56 | 1.54 |

Table 4.5: Line Ratios for Optically Thin Lines taken from the center of line

# Chapter 5

# Conclusion

In this thesis, ten $H_2O$ lines observable by the Herschel Space Observatory are modeled from intermediate mass star formation regions. Nine protostellar envelopes were modeled under conditions of spherical symmetry, zero systematic velocity field, a density power law with index 1.5, a dust to gas mass ratio of 1:100, and a total optical depth through the center of the cloud at 100 microns of 0.1. Each model is described by an envelope mass and its protostar luminosity. Luminosities of $L = 100L_\odot$, $L = 500L_\odot$, and $L = 1000L_\odot$ were chosen for the protostars, and masses $M = 10M_\odot$, $M = 100M_\odot$, and $M = 500M_\odot$ were chosen for the envelopes. Temperature profiles, temperature as a function of radius, for each model were obtained using the program DUSTY. Molecular hydrogen and water densities of each model were then created using a 1.5 power law index and an abundance of $H_2O$ relative to $H_2$ of $1 \times 10^{-7}$ was used. Furthermore, water completely freezes out on dust grains at $T = 20K$ and cooler and does not contribute to the molecular emission.

The molecular emission was obtained from RATRAN, a program which consists of two sub-programs, AMC and SKY. The AMC program calculated the level populations of the molecule throughout the profile of the region that was supplied as input by calculating the radiative transfer using an accelerated Monte Carlo method. For a given frequency, the SKY program determines the source function at every position in the model and traces all of its rays and determines its emission distribution and outputs the data as a FITS image. The FITS images were convolved to an appropriate Herschel beam size and its spectral profiles was obtained. For every model, ten $H_2O$ lines profiles were obtained.

From the models, all water lines suffer from a large amount of beam dilution. This beam dilution is due to the fact that these regions are located 1 kpc away from Earth and that Herschel's beam sizes are always much greater than the emitting surface of that region (eg. $\tau_\nu = 2/3$). In comparison to similiar studies modeling water emission from star formation regions our line strengths are roughly two orders of magnitude weaker, but line profiles are the same. The differences in line strengths are attributed to distance and beam dilution when comparing to the low mass

star formation regions. For high mass star formation regions, the differences are attributed to stronger water emission in the high mass model because the protostar's luminosity is much larger.

It is evident that the $H_2O$ lines are great luminosity probes but poor envelope mass probes. Out of all ten lines, only 2 have relatively strong line strengths ( 0.1 K). These are the high excitation line $3_{21} - 3_{12}$ and the low excitation line $2_{12} - 2_{01}$. All integrated line intensities, and line ratios of optically thin lines are strongly correlated with the protostar's luminosity. Envelope mass can still be determined from the analysis of optically thick water lines, but is much more difficult. This is because all of our line ratios, line strengths, and integrated intensities show no consistent trends with varying envelope mass. More mass simply goes in the outer envelope where the water is frozen and does not contribute to the water emission and absorption.

The difficulty in an envelope mass determination of an intermediate mass protostar is compounded by the fact there is only 1 relatively strong optically thick line at 1000 pc (where the candidate intermediate mass protostars are detected). For future observations of these lines with Herschel, line strengths, line ratios at $0 kms^{-1}$, and line ratios of $T_{MB(peak)}/T_{MB(absorption)}$ of optically thick lines can be compared to the ones tabulated in this research, if the observations are viable, to help determine a protostar's envelope mass. The more lines observed, the better the determination of a protostar's envelope mass.

Even though there are not many strong water lines available for intermediate mass star formation regions at 1000 pc, the limited information that can be given by the strong lines is great. Verifications of line strengths, profile types, and the absence of line detections give insight into the environments of these regions. The determination of whether or not these models successfully replicate the regions that exist in our galaxy is profound. We have modeled these regions under a particular set of conditions, for example spherical symmetry and a power law index of 1.5 (describes a zero systematic velocity field) and the observations of these lines will pull into question these very conditions. Ultimately, the water line observations will provide us with much environmental information regarding star formation regions. Furthermore, they will shed light upon many long outstanding questions about the star formation process which are told by their envirnomental conditions that has since been shielded from us.

## 5.1 Future Work

It has been found that individual water lines do not successfully probe the mass of the protostellar envelopes in our models. This is due to the fact that for our models with different envelope mass the density throughout the regions is roughly the same for all nine models. Also, by increasing the envelope mass more water is effectively deposted in the freezeout zone. Therefore, for future work instead of using source

luminosity and envelope mass as our two parameters of investigation one should use source luminosity and density. Appropriate choices of $\tau_{100}$ would be 0.1,0.05 and 0.01. This will change the normalization of the density profiles. Consequently, the normalizations of the density profiles will be separated by a larger amount in comparision to the density profiles of our current models. In effect, these changes to the density profiles will change the level populations throughout a region's profile and the line strengths and line profiles associated to a particular transition.

# Appendix

## Interpolation Fortran Code

```
C
C
C This program is intended for convert Dusty2.06's output
C .rtb formats into Ratran's required input model .mdl.
C
C
C


      CHARACTER*255 infilename,outfilename
      REAL*4 y(200),eta(200),u(200),tauF(200),eps(200),T(200)
      REAL*4 density(200),y2_density(600),y2_T(600),rho(600)
      REAL y_gap,fraction,T_freezout,db,tau,opacity,r1,scaled
      LOGICAL file_exists

C open Dusty's 2.06 input file

   9  WRITE(6,10)
  10  FORMAT('Name of Dusty2.06 output file? >> ',$)
      READ(5,12)infilename
  12  FORMAT(A)
      INQUIRE(FILE=infilename,EXIST=file_exists)
      IF (.NOT.file_exists) THEN
         WRITE(6,*)'file does not exist. Please try again....'
         GOTO 9
        ENDIF
      OPEN(1,FILE=infilename)

C open the output file (.mdl)

  20  WRITE(6,21)
```

```
 21   FORMAT('Name of the desired output file? >> ',$)
      READ(5,12)outfilename
      INQUIRE(FILE=outfilename,EXIST=file_exists)
      IF (file_exists) THEN
         WRITE(6,*)'file already exists, try again....'
         GOTO 20
        ENDIF
      OPEN(2,FILE=outfilename)

C input necessary model parameters

      WRITE(6,100)
 100  FORMAT('The fractional abundance of water isotopomer? >>',$)
      READ(5,*)fraction
      WRITE(6,101)
 101  FORMAT('temperature where all water freezes out? >> ',$)
      READ(5,*)T_freezout
      WRITE(6,110)
 110  FORMAT('velocity width (1/e half-width)? >>',$)
      READ(5,*)db
      WRITE(6,120)
 120  FORMAT('The optical depth of the interstellar cloud? >>',$)
      READ(5,*)tau
      WRITE(6,130)
 130  FORMAT('Opacity of the envelope (cm2 g-1)? >>',$)
      READ(5,*)opacity
      WRITE(6,140)
 140  FORMAT('Radius at which dust sublimates (r1-m)? >>',$)
      READ(5,*)r1
      WRITE(6,145)
 145  FORMAT('Outer scaled Radius? >>',$)
      READ(5,*)scaled

C write the header for the output file

C read the and throw away junk belonging to .rtb file

      READ(1,12)infilename
      READ(1,12)infilename
      READ(1,12)infilename
C      READ(1,12)infilename ! remove this line if need be (sometimes dusty writes 2

C reading and manipulating input file data

      READ(1,*)
```

```
      DO i=1,200
          READ(1,*,END=150)y(i),eta(i),u(i),tauF(i),eps(i),T(i)
          R=((r1*100)**(-0.5)-(scaled*r1*100)**(-0.5))
          O=(50*tau)/(2*opacity*(y(i)*r1*100)**(1.5)*(1.67E-24))
          density(i)=O/R
         ENDDO

C the variable y below is the normalized radius - Dusty Output parameter

 150  number_input_cells=i-1
      WRITE(6,160)number_input_cells,y(1),+ y(number_input_cells)
 160  FORMAT('input file has ',I3,' cells.',
     + /'the innermost cell extends to ',G12.4,' (y)',
     + /'the outer radius is at ',G12.4,' (y)',
     + /'choose the size of an inner gap (y - < 1.0) >> ',$)
      READ(5,*)y_gap
      WRITE(6,170)
 170  FORMAT('number of cells to interpolate between input',
     + ' positions >> ',\$)
      READ(5,*)number_interp

      WRITE(2,200)y(number_input_cells)*r1,
     + (number_interp+1)*(number_input_cells-1) + 2
 200  FORMAT('# object is ',/'#',/'#',/'rmax=',E9.3,/'ncell=',I4.4,
     + /'tcmb=2.728',/'columns=id,ra,rb,nh,nm,tk,td,db,vr',
     + /'gas:dust=100',/'@')
      WRITE(2,250)1,0.0,y_gap*r1,0,0,100.,100.,db

C  setup the spline interpolation scheme

      CALL SPLINE(y,density,number_input_cells,
     + 1.0E31,1.0E31,y2_density)
      CALL SPLINE(y,T,number_input_cells,
     + 1.0E31,1.0E31,y2_T)

C  first write the innermost shell (just outside of the inner gap)
      ra=y_gap*r1
      rb=y(1)*r1
      WRITE(2,250)2,ra,rb,density(1),fraction*density(1),T(1),T(1),db
      ra_AU=y(2)
      ra=rb

C using the interpolation scheme starting with cell=3

      ncell=3
```

```
      DO i=2,number_input_cells
          dr=(y(i)-y(i-1))/FLOAT(number_interp+1)
          DO j=1,number_interp+1
             rb_AU=ra_AU + dr
             CALL SPLINT(y,density,y2_density,
     +        number_input_cells,rb_AU,density_rb)
             CALL SPLINT(y,T,y2_T,number_input_cells,rb_AU,T_rb)
C             rho(i)=density_rb
             rb=rb_AU*r1
C             M=(50*tau)/(2*opacity*(ra*100)**(1.5)*(1.67E-24))
C             M=(50*0.1)/(2*86.5*(1.67E-24))
C             L=(ra*100)**(1.5)
             rho(i)=(1.730642E+22)/((ra*100)**(1.5)*R)
             WRITE(6,*)rho(i)
             IF (T_rb.GT.T_freezout) THEN
                WRITE(2,250)ncell,ra,rb,rho(i),fraction*rho(i),T_rb
     +           ,T_rb,db
 250             FORMAT(I4,1P,4(1X,E13.7),0P,2(1X,E11.5),1X,F3.1,
     +           ' 0.0')
               ELSE
                WRITE(2,250)ncell,ra,rb,rho(i),fraction*rho(i)*1E-05,
     +            T_rb,T_rb,db
               ENDIF
             ra_AU=rb_AU
             ra=rb
             ncell=ncell+1
            ENDDO

         ENDDO
      CLOSE(1)
      CLOSE(2)
      STOP
      END

      FUNCTION LENGTH(CHARNAME)
C
C  FIND THE LENGTH OF A CHARACTER VARIABLE
C
C  FIND THE LENGTH OF THE CHARACTER NAMED 'CHARNAME'. ALL
C  BLANKS ON THE RIGHT ARE STRIPPED OFF AND THE LENGTH OF THE
C  RESULTING STRING IS RETURNED.
C
C  THIS ROUTINE HAS BEEN FOOLED BY SOME STRINGS WHICH HAVE STRANGE UNPRINTABLE
C  CHARACTERS INSTEAD OF BLANKS.  THESE DO NOT SHOW UP WHEN THE STRING IS
C  PRINTED BUT DO EXIST AND THUS ARE NOT REMOVED BY THIS PROGRAM.  THIS MEANS
```

```
C  IT GIVES THE WRONG LENGTH.
C
C  MIKE FICH, BERKELEY, FEB 1982.
C
      CHARACTER*(*) CHARNAME
      CHARACTER*1 BLANK
      BLANK=' '
      J=LEN(CHARNAME)
      DO 100 I=1,J
          LENGTH=J-I+1
          IF(CHARNAME(LENGTH:LENGTH).NE.BLANK) RETURN
 100     CONTINUE
      LENGTH=0
      RETURN
      END

      SUBROUTINE SPLINE(X,Y,N,YP1,YPN,Y2)
      PARAMETER (NMAX=600)
      REAL*4 X(N),Y(N),Y2(N),U(NMAX)
      IF (YP1.GT..99E30) THEN
        Y2(1)=0.
        U(1)=0.
      ELSE
        Y2(1)=-0.5
        U(1)=(3./(X(2)-X(1)))*((Y(2)-Y(1))/(X(2)-X(1))-YP1)
      ENDIF
      DO 11 I=2,N-1
        SIG=(X(I)-X(I-1))/(X(I+1)-X(I-1))
        P=SIG*Y2(I-1)+2.
        Y2(I)=(SIG-1.)/P
        U(I)=(6.*((Y(I+1)-Y(I))/(X(I+1)-X(I))-(Y(I)-Y(I-1))
     *      /(X(I)-X(I-1)))/(X(I+1)-X(I-1))-SIG*U(I-1))/P
11    CONTINUE
      IF (YPN.GT..99E30) THEN
        QN=0.
        UN=0.
      ELSE
        QN=0.5
        UN=(3./(X(N)-X(N-1)))*(YPN-(Y(N)-Y(N-1))/(X(N)-X(N-1)))
      ENDIF
      Y2(N)=(UN-QN*U(N-1))/(QN*Y2(N-1)+1.)
      DO 12 K=N-1,1,-1
        Y2(K)=Y2(K)*Y2(K+1)+U(K)
12    CONTINUE
      RETURN
```

```
      END
      SUBROUTINE SPLINT(XA,YA,Y2A,N,X,Y)
      DIMENSION XA(N),YA(N),Y2A(N)
      KLO=1
      KHI=N
1     IF (KHI-KLO.GT.1) THEN
        K=(KHI+KLO)/2
        IF(XA(K).GT.X)THEN
          KHI=K
        ELSE
          KLO=K
        ENDIF
      GOTO 1
      ENDIF
      H=XA(KHI)-XA(KLO)
      IF (H.EQ.0.) PAUSE 'Bad XA input.'
      A=(XA(KHI)-X)/H
      B=(X-XA(KLO))/H
      Y=A*YA(KLO)+B*YA(KHI)+
     *      ((A**3-A)*Y2A(KLO)+(B**3-B)*Y2A(KHI))*(H**2)/6.
      RETURN
      END
```

# References


[1] M. T. Beltran, R. Estalella, J. M. Girart, P. T. P. Ho, and G. Anglada. On the nature of outflows in the intermediate-mass protostars: a case study of iras 20050+2720. *A&A*, 481:93–105, 2008.

[2] John H. Black. Energy budgets of diffuse clouds. *The First Symposium on the Infrared Cirrus and Diffuse Interstellar Clouds ASP Conference Series*, 58, 1994.

[3] A.M.S. Boonman, S.D. Doty, E.F. van Dishoeck, E.A. Bergin, G.J. Melnick, C.M. Wright, and R. Stark. Modeling gas-phase $h_2o$ between 5 $\mu m$ and 540 $\mu m$ toward massive protostars. *A&A*, 406:937–955, 2003.

[4] Bradley W. Carroll and Dale A. Ostlie. *An Introduction to Modern Astrophysics*. Addison-Wesley Publishing Company, Inc., 1996.

[5] Thijs de Graauw, Nick Whyborn, Emmanuel Caux, Tom Phillips, Juergen Stutzki, Xander Tielens, Rofl Gusten, Frank Helmich, W. Luinge, John Pearson, Peter Roelfsema, Rudolf Schieder, Klaas Wildeman, and Kees Wafelbakker. The herchel-heterodyne instrument for the far-infrared (hifi). *American Astronomical Society Meeting 207 #35.03 Bulletin of the American Astronomical Society*, 37:1219, 2005.

[6] S.D. Doty, F.F.S. van der Tak, E.F. van Dishoeck, and A.M.S. Boonman. Water line strengths toward high-mass star forming regions: Predictions for herschel/hifi. *Protostars and Planets V, Proceedings of the Conference*, page LPI Contribution No. 1286. 8537, October 24–28 2005.

[7] D.R.Poelman and F.F.S. van der Tak. Modeling the water line emission from the high-mass star-formation region afgl 2591. *astro-ph*, page arXiv:0710.1503v1, 2007.

[8] A. Fuente, R. Neri, and P. Caselli. Detection of a hot core in the intermediate-mass class 0 protostar ngc 7129-firs 2. *A&A*, 444:481–493, 2005.

[9] M.R. Hogerheijde and F.F.S. van der Tak. An accelerated monte carlo method to solve two-dimensional radiative transfer and molecular excitation. *A&A*, 362:697–710, 2000.

[10] Zeljko Ivezic and Moshe Elitzur. Self-similiarity and scaling behaviour of infrared emission from radiatively heated dust-i. theory. *Mon. Not. R. Astron. Soc*, 287:799–811, 1997.

[11] M. F. Kessler, J.A. Steinz, M.E. Anderegg, J. Clavel, G. Drechsel, P. Estaria, J. Faelker, J.R. Riedinger, A. Robson, B.G. Taylor, and S. Ximenez de Ferran. The infrared space observatory (iso) mission. *A&A*, 315:L27–L31, 1996.

[12] H.W. Kroto. *Molecular Rotational Spectra*. Dover Publications, Inc., New York, 1992.

[13] Jesus Martin-Pintado, Izaskun Jimenez-Serra, and Arturo Rodriguez-Franco. A new intermediate-mass protostar in the cepheus a hw2 region. *The Astrophysical Journal*, 628:L61–L64, 2005.

[14] J.S. Mathis, W. Rumpl, and K.H. Nordsieck. The size distribution of interstellar grains. *The Astrophysical Journal*, 217:425, 1977.

[15] Gary J. Melnick, Volker Tolls, David A. Neufeld, Yuan Yuan, Paule Sonnentrucker, Dan M. Wilson, Edwin A. Bergin, and Michael J. Kaufman. Detection of extended hot water in the outflows from ngc 2071. *astro-ph*, page arXiv:0805.0573v1, 2008.

[16] Francesco Palla and Steven W. Stahler. The evolution of intermediate-mass protostars. i. basic results. *The Astrophysical Journal*, 375:288–299, 1991.

[17] D. R. Poelman, M. Spaans, and A. G. G. M. Tielens. The interpretation of water emission from dense interstellar clouds. *A&A*, 464:1023–1027, 2007.

[18] J.M. Rathborne, R. Simon, and J. M. Jackson. The detection of protostellar condensations in infrared dark cloud cores. *The Astrophysical Journal*, 662:1082–1092, 2007.

[19] F. H. Shu. Self-similar collapse of isothermal spheres and star formation. *The Astrophysical Journal*, 214:488, 1997.

[20] F.F.S. van der Tak, C.M. Walmsley, F. Herpin, and C. Ceccarelli. Water in the envelopes and disk around young high-mass stars. *astro-ph*, pages arXiv:astro–ph/0510640v1, 2005.

[21] T.A. van Kempen, S.D. Doty, E.F. van Dishoeck, M.R. Hogerheijde, and J.K. Jorgensen. Modeling water emission from low-mass protostellar envelopes. *astro-ph*, page arXiv:0805.0772v1, 2008.

[22] C.D. Wilson, R.S. Booth, A.O.H. Olofsson, M. Olberg, C.M. Persson, Aa. Sandqvist, A. Hjalmarson, V. Buat, P.J. Encrenaz, M. Fich, U. Frisk, M. Gerin, G. Rydback, and T. Wiklind. Upper limits to the water abundance in starburst galaxies. *astro-ph*, pages arXiv:astro–ph/0703632v2, 2007.